



# Mn–Cr ages and formation conditions of fayalite in CV3 carbonaceous chondrites: Constraints on the accretion ages of chondritic asteroids

Kaori Jogo<sup>a,\*</sup>, Tomoki Nakamura<sup>b</sup>, Motoo Ito<sup>c</sup>, Shigeru Wakita<sup>d</sup>,  
Mikhail Yu. Zolotov<sup>e</sup>, Scott R. Messenger<sup>f</sup>

<sup>a</sup> Division of Earth-System Sciences, Korea Polar Research Institute, 26 Songdomirae-ro, Yeonsu-gu, Incheon 406-840, South Korea

<sup>b</sup> Department of Earth and Planetary Material Sciences, Faculty of Science, Tohoku University, Aoba, Sendai, Miyagi 980-8578, Japan

<sup>c</sup> Kochi Institute for Core Sample Research, JAMSTEC B200 Monobe, Nankoku, Kochi 783-8502, Japan

<sup>d</sup> Center for Computational Astrophysics, National Astronomical Observatory of Japan, 2-21-1 Osawa, Mitaka, Tokyo 181-8588, Japan

<sup>e</sup> School of Earth and Space Exploration, Arizona State University, Tempe, AZ 85287-1404, USA

<sup>f</sup> Robert M. Walker Laboratory for Space Science, NASA Johnson Space Center, ARES, Mail Code KR, 2101 NASA Parkway, Houston, TX 77058, USA

Received 24 July 2015; accepted in revised form 16 November 2016; available online 21 November 2016

## Abstract

Chondritic planetesimals are among the first planetary bodies that accreted inside and outside water snow line in the protoplanetary disk. CV3 carbonaceous chondrite parent body accreted relatively small amount of water ice, probably near the snow line, and experienced water-assisted metasomatic alteration that resulted in formation of diverse secondary minerals, including fayalite (Fa<sub>80–100</sub>). Chemical compositions of the CV3 fayalite and its Mn–Cr isotope systematics indicate that it formed at different temperature (10–300 °C) and fluid pressure (3–300 bars) but within a relatively short period of time. Thermal modeling of the CV3 parent body suggests that it accreted ~3.2–3.3 Ma after CV3 CAIs formation and had a radius of >110–150 km. The inferred formation age of the CV3 parent body is similar to that of the CM2 chondrite parent body that probably accreted beyond the snow line, but appears to have postdated accretion of the CO and ordinary chondrite parent bodies that most likely formed inside the snow line. The inferred differences in the accretion ages of chondrite parent bodies that formed inside and outside snow line are consistent with planetesimal formation by gravitational/streaming instability. © 2016 Elsevier Ltd. All rights reserved.

**Keywords:** Aqueous alteration; Fayalite; CV3 carbonaceous chondrites; Mn–Cr method; Age determination; Equilibrium thermodynamics; Thermal modeling

## 1. INTRODUCTION

About 4.6 billion years ago, the Solar System began as a solar nebula consisting mainly of hydrogen gas and minor amounts of dust. At or beyond the water ice evaporation front known as the water snow line (hereafter snow line)

(Hayashi, 1981; Stevenson and Lunine, 1988; Cyr et al., 1998; Cuzzi and Zahnle, 2004; Ciesla and Cuzzi, 2006), water existed as vapor, ice and hydrates. Accretion of dust, vapor, ice and hydrates formed primitive bodies (planetesimals), which further aggregated into larger planetary embryos and planets. Small terrestrial planets formed inside the water snow line and are volatile depleted, while the gas-giant planets formed outside the snow line. This suggests that planet formation processes inside and outside the snow

\* Corresponding author. Fax: +82 (0)32 760 5497.

E-mail address: [kaorijogo@kopri.re.kr](mailto:kaorijogo@kopri.re.kr) (K. Jogo).

line could have been different. Understanding the earliest histories of planetesimals formed near the snow line can reveal unique insights into this critical transition zone between the inner and outer early Solar System.

Chondritic meteorites (chondrites) are fragments of planetesimals that preserve records of their origins and evolutionary histories. Isotopic and petrological studies of minerals in chondrites constrain both the timescales and physical–chemical conditions of their formation. Chondrites are currently classified into fifteen groups based on their bulk chemical and isotopic compositions and petrographic characteristics. Each group may represent a different parent body, formed in a distinct nebular region and/or at a particular time (e.g., Zolensky and McSween, 1988; Wood, 2005; Brearley, 2006; Krot et al., 2006; Rubin, 2010, 2011). The differences in bulk elemental abundances and volatile contents among chondrite groups are thought to reflect radial variations in the temperature and composition of the nebular gas and the abundances of dust, chondrules, and Ca–Al-rich inclusions (CAIs). The relative heliocentric distances of the formation regions of different chondrite groups have been inferred from their petrographic properties, chemical and isotope compositions, and volatile contents (e.g., Rubin and Wasson, 1995; Wood, 2005; Rubin, 2010, 2011). Rubin (2010, 2011) proposed that the forming regions of chondrite groups could be ordered as EH–EL, OC, R, CR, CV–CK, CM–CO, and CI with increasing heliocentric distance. More recently, van Kooten et al. (2016) proposed that CR chondrite parent body formed further from the Sun than other chondrite parent bodies because of its high abundances of presolar grains and primordial  $\delta^{54}\text{Cr}$  and  $\delta^{26}\text{Mg}$  isotopic signatures. The small amount of secondary minerals and volatile components in CV chondrites may suggest their parent body accreted just beyond the snow-line (e.g., Wood, 2005).

CV3 chondrites are divided into three subgroups, the oxidized Allende-like (CV3<sub>OxA</sub>), the oxidized Bali-like (CV3<sub>OxB</sub>) and the reduced (CV3<sub>Red</sub>) type, based on their mineralogy, petrology and bulk chemical and isotopic compositions (McSween, 1977; Weisberg et al., 1997). The CV3<sub>OxB</sub> chondrites experienced aqueous alteration that resulted in formation of secondary fayalite, ferroan olivine, phyllosilicate, magnetite, Fe,Ni–sulfide, Fe,Ni–carbide, salite-hedenbergite pyroxenes, and andradite (Krot et al., 2004). The CV3<sub>OxA</sub> chondrites experienced relatively high-temperature Fe-alkali-halogen metasomatic alteration (Brearley, 1997, 1999; Bonal et al., 2006) that resulted in formation of secondary ferroan olivine, nepheline, sodalite, andradite, grossular, wollastonite, kirschsteinite, and salite-hedenbergite pyroxenes (Kimura and Ikeda, 1995; Ikeda and Kimura, 1995; Krot et al., 1995, 1998, 2004). The CV3<sub>Red</sub> chondrites experienced similar metasomatic alteration to that of the CV3<sub>OxA</sub> chondrites, but to a smaller degree (Krot et al., 1995, 1998, 2004).

Secondary fayalite can be used to constrain the timescales and hydrothermal evolutionary processes of the CV3 parent body. In particular, the chemical compositions of fayalite reflect the physical–chemical conditions within the parent body during aqueous alteration (Hua and Buseck, 1995; Krot et al., 1998; Choi et al., 2000; Hua

et al., 2005; Zolotov et al., 2006; Jogo et al., 2009). Near-pure fayalite ( $\text{Fa}_{>90}$ ,  $\text{Fa} = \text{Fe}/(\text{Fe} + \text{Mg}) \times 100 \text{ mol}\%$ ) occurs only in the CV3<sub>OxB</sub> chondrites and CV3<sub>OxB</sub> clasts in CV3<sub>Red</sub> chondrites (Krot et al., 2000; Tomeoka and Tanimura, 2000; Jogo et al., 2009). In addition, fayalite is suitable for  $^{53}\text{Mn}$ – $^{53}\text{Cr}$  dating ( $^{53}\text{Mn}$  decays to  $^{53}\text{Cr}$  with a half-life of 3.7 million years) due to its high Mn/Cr ratios (Hutcheon et al., 1998; Hua et al., 2005; Jogo et al., 2009).

The formation timescales and aqueous alteration conditions inferred from the analyses of secondary fayalite can yield further constraints on the accretion timing of CV3 chondrites. Such inferences are made by constructing thermal evolutionary models that successfully account for the timing and the conditions of aqueous alteration constrained by fayalite. The thermal history of a parent body is a function of the  $^{26}\text{Al}$  abundance, water ice/rock ratio and parent body size. In thermal models for the CV3 parent body, different values for parameters such as peak temperature,  $^{26}\text{Al}$  content, and water/rock ratios have been used. As a result, various evolutionary processes of CV3 bodies were proposed (Travis and Schubert, 2005; Palguta et al., 2010; Elkins-Tanton et al., 2011; Fu and Elkins-Tanton, 2014). Details are discussed in the Section 4.2.

Here we present results of chemical and Mn–Cr isotopic analyses of fayalite in CV chondrites and derive constraints on the thermal and physical evolution of the CV chondrite parent body. We performed detailed mineralogical and chemical investigations of fayalite in four CV3 chondrites; CV3<sub>OxB</sub> clasts in CV3<sub>Red</sub> Asuka 881317 (A881317), CV3<sub>OxB</sub> Yamato 86009 (Y86009), CV3<sub>OxB</sub> Meteorite Hills 00430 (MET00430) and CV3<sub>OxB</sub> MET01074, and estimated temperature and fluid pressure conditions of its formation. We determined formation ages of fayalite in these chondrites based on *in-situ* Mn–Cr isotopic measurements using ion microprobes and modeled the thermal evolution of the CV3<sub>OxB</sub> chondrite parent body. A comparison of formation conditions and ages of fayalite with evolutionary models allowed us to constrain the accretion time, size and early history of the CV3 parent body.

## 2. MATERIAL AND METHODS

### 2.1. Sample description

Chemical compositions, mineralogical and petrological characterization of fayalite in A881317, Y86009, MET00430 and MET01074 chondrites, were obtained by scanning electron microscopy (SEM), field emission scanning electron microscopy (FE-SEM) and electron microprobe (EPMA). A 25 nm-thick carbon film was applied to the sample surfaces prior to SEM, FE-SEM and EPMA analyses in order to eliminate the electrostatic charge. The SEM (JEOL-5800LV at Kyushu University and JSM-6610 at Korea Polar Research Institute) was equipped with a backscattered electron (BSE) imaging system and an energy dispersive X-ray spectrometer. X-ray spectra were obtained at 15 keV accelerating voltage and 0.5 nA beam current to identify minerals. To observe micro-textures in fayalite and other secondary minerals associated with fayalite, we used the FE-SEM (JSM-7000F at University of

Tokyo), operated at 15 keV accelerating voltage and 0.3 nA beam current. Chemical compositions of fayalite and other minerals were obtained using the EPMA (JEOL JXA733 at Kyushu University) equipped with a wavelength-dispersive X-ray spectrometer. Quantitative chemical analyses were operated at 15 kV accelerating voltage and 10 nA beam current. ZAF correction method was applied. Detection limits are 0.05 wt.% for elements analyzed, and the reproducibility is less than 5% of concentrations of each element on the basis of the repeated analysis of the standard minerals.

## 2.2. Mn–Cr isotope measurements

Mn–Cr isotopic measurements were performed with the Cameca ims-6f SIMS at Kyushu University and the NanoSIMS 50L at NASA Johnson Space Center. SIMS measurements were performed during three sessions: large fayalite grains (20–50  $\mu\text{m}$ ) in Y86009 clast 1 were measured by Cameca ims-6f SIMS [session 1]; small fayalite grains (10–20  $\mu\text{m}$ ) in clasts 2, 4, 7, 8, 9 and 14, and host in Y86009 [session 2], and those in all clasts in A881317, MET00430 and MET01074 [session 3] were analyzed by NanoSIMS 50L. CV3 fayalite grains have high Mn/Cr ratios ( $^{55}\text{Mn}/^{52}\text{Cr} = 6 \times 10^2 - 4 \times 10^5$ , MnO = 0.6–1.3 wt %;  $\text{Cr}_2\text{O}_3 < 0.05$  wt%) that are suitable for the Mn–Cr isotopic measurements. We also measured olivine and pyroxene with low Mn/Cr ratios ( $^{55}\text{Mn}/^{52}\text{Cr} < 1$ ) in chondrules or matrices near the measured fayalite to determine the ( $^{53}\text{Cr}/^{52}\text{Cr}$ ) intercept. Although fayalite and chondrule silicates are not co-genetic, the inferred initial  $^{53}\text{Cr}/^{52}\text{Cr}$  ratio is within the uncertainty of SIMS measurements.

In ims-6f SIMS measurements [session 1], we used a focused  $^{16}\text{O}^-$  primary beam  $\sim 20 \mu\text{m}$  in diameter and 0.2–0.9 nA current. The primary  $^{16}\text{O}^-$  ions were accelerated with +12 keV to sputter the sample surface. Positive secondary ions were accelerated with  $-4.5$  keV and sampled with a 100 eV energy window. The mass resolving power ( $M/\Delta M$ ) was  $\sim 3000$  was sufficient to resolve [ $^{24}\text{Mg}^{28}\text{Si}$ ] $^+$  from  $^{52}\text{Cr}^+$ , [ $^{25}\text{Mg}^{28}\text{Si}$ ] $^+$  and [ $^{26}\text{Mg}^{27}\text{Al}$ ] $^+$  from  $^{53}\text{Cr}^+$ , and [ $^{28}\text{Si}^{27}\text{Al}$ ] $^+$  from  $^{55}\text{Mn}^+$ , but was not sufficient to resolve [ $^{52}\text{CrH}$ ] $^+$  from  $^{53}\text{Cr}^+$  or [ $^{54}\text{FeH}$ ] $^+$  from  $^{55}\text{Mn}^+$ . Hutcheon et al. (1998) and Hua et al. (2005) showed that the contributions of the hydride to  $^{53}\text{Cr}^+$  was  $< 1\%$  and the hydrides of  $^{55}\text{Mn}$  totaled less than 1%, and consequently hydrides could be neglected. Detailed measurement conditions are described in Jogo et al. (2009).

In NanoSIMS 50L measurements [sessions 2 and 3], a focused 16 keV  $^{16}\text{O}^-$  primary ion beam was rastered over  $3 \times 3$  or  $5 \times 5 \mu\text{m}^2$  areas of the sample surface. Primary ion beam currents ranged from 15–60 pA for terrestrial standards to 250–400 pA for fayalite in meteorites. We verified that the measured  $^{53}\text{Cr}/^{52}\text{Cr}$  and  $^{55}\text{Mn}/^{52}\text{Cr}$  ratios of the standards were invariable with primary beam current, within error. The secondary mass spectrometer was operated at 8 keV with a 20 eV energy window. Secondary ions of  $^{25}\text{Mg}^+$ ,  $^{29}\text{Si}^+$ ,  $^{52}\text{Cr}^+$ ,  $^{53}\text{Cr}^+$ ,  $^{55}\text{Mn}^+$  and  $^{57}\text{Fe}^+$  were acquired simultaneously in multi-collection mode with electron multipliers at a high mass resolution of  $\sim 8000$  (CAMECA NanoSIMS definition). Secondary ion intensi-

ties were corrected for QSA effects and dead time (44 ns). One analysis consists of 100–300 cycles (10–30 blocks) of the measurement set in all secondary ions 8–41 s. Each run started after stabilization of the secondary ion beam intensity following pre-sputtering of  $\sim 30$  min. We used elemental images of  $^{25}\text{Mg}^+$  and  $^{57}\text{Fe}^+$  to identify small fayalites (5–30  $\mu\text{m}$ ) in chondrules and matrix (Fig. 1). After SIMS measurements, the samples were examined by SEM to verify that the ion beam hit the right spots.

## 2.3. Mn/Cr relative sensitivity factor and instrumental mass fractionation

San Carlos olivine ( $\text{Fa}_{11}$ ) was measured as a standard, not fayalite, to determine the Mn/Cr relative sensitivity factor (RSF; defined as  $(^{55}\text{Mn}/^{52}\text{Cr})_{\text{true}} / (^{55}\text{Mn}/^{52}\text{Cr})_{\text{SIMS}}$ ) and the instrumental mass fractionation (IMF; defined as  $(^{53}\text{Cr}/^{52}\text{Cr})_{\text{true}} / (^{53}\text{Cr}/^{52}\text{Cr})_{\text{SIMS}}$ ) for SIMS ims-6f and NanoSIMS analyses.

In the SIMS ims-6f measurements [session 1],  $^{55}\text{Mn}^+ / ^{52}\text{Cr}^+$  ratios were stable only for San Carlos olivine standard during a single measurement; the  $^{55}\text{Mn}^+ / ^{52}\text{Cr}^+$  showed various trends with time for meteoritic fayalite (e.g., Supplementary Fig. S1). We selected specific cycles which had stable  $^{55}\text{Mn}^+ / ^{52}\text{Cr}^+$  ratios, and then calculated the  $^{55}\text{Mn}/^{52}\text{Cr}$  as the average of the  $^{55}\text{Mn}^+ / ^{52}\text{Cr}^+$  values in selected cycles. The errors on the  $^{55}\text{Mn}/^{52}\text{Cr}$  were evaluated as two standard deviations of the  $^{55}\text{Mn}^+ / ^{52}\text{Cr}^+$  values. The measured  $^{55}\text{Mn}/^{52}\text{Cr}$  ratio was corrected for RSFs using the  $^{55}\text{Mn}/^{52}\text{Cr}$  ratios of San Carlos olivine by SIMS and those by ICP-AES (Inductively Coupled Plasma Atomic Emission Spectrometry; Seiko SPS-1200AR at Kyushu University, Jogo et al., 2009). The RSF values are 1.14–1.17.

In contrast, the  $^{53}\text{Cr}^+ / ^{52}\text{Cr}^+$  ratios were stable for San Carlos olivine standard and meteoritic fayalite during a single measurement in the SIMS ims-6f analysis [session 1] (e.g., Supplementary Fig. S1). We selected the same cycles, in which  $^{55}\text{Mn}^+ / ^{52}\text{Cr}^+$  were stable, and then calculated the  $^{53}\text{Cr}/^{52}\text{Cr}$  of the meteoritic fayalite as the average of the  $^{53}\text{Cr}^+ / ^{52}\text{Cr}^+$  values in selected cycles. The errors on the  $^{53}\text{Cr}/^{52}\text{Cr}$  were evaluated as two standard deviations of the mean of the  $^{53}\text{Cr}^+ / ^{52}\text{Cr}^+$  value in each cycle ( $(^{53}\text{Cr}/^{52}\text{Cr})_{\text{error}} = (\text{two standard deviation of the } ^{53}\text{Cr}^+ / ^{52}\text{Cr}^+ \text{ value in each cycle}) / (\text{block number})^{1/2}$ ). The  $^{53}\text{Cr}/^{52}\text{Cr}$  ratio was corrected for IMF using the  $^{53}\text{Cr}/^{52}\text{Cr}$  ratio in San Carlos olivine and the published value for terrestrial chromium of 0.113459 (Papanastassiou, 1986). The IMF values are 0.99–1.00.

In the NanoSIMS measurements [sessions 2 and 3], the  $^{55}\text{Mn}^+ / ^{52}\text{Cr}^+$  isotopic compositions were either stable or increased with time for San Carlos olivine standards during a single measurement; they showed various trends with time for meteoritic fayalite (e.g., Supplementary Fig. S2). The  $^{53}\text{Cr}^+ / ^{52}\text{Cr}^+$  isotopic compositions were stable for San Carlos olivine standards and meteoritic fayalite during a single measurement. We calculated the  $^{55}\text{Mn}/^{52}\text{Cr}$  and  $^{53}\text{Cr}/^{52}\text{Cr}$  of the meteoritic fayalite using the same methods used for ims-6f SIMS data reduction. The measured  $^{55}\text{Mn}/^{52}\text{Cr}$  ratio was corrected for RSF using the

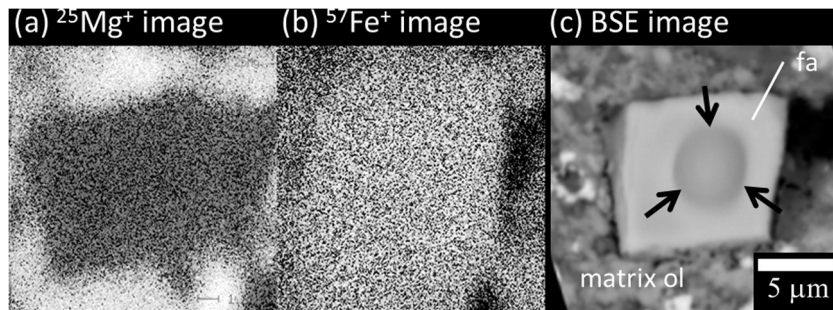


Fig. 1.  $^{25}\text{Mg}^+$  and  $^{57}\text{Fe}^+$  isotopic images (a and b) and a BSE image (c) of the same fayalite (fa), which is embedded in the fine-grained matrix olivine (matrix ol). (a and b)  $^{25}\text{Mg}^+$  and  $^{57}\text{Fe}^+$  isotopes are rich in a bright area, and rare in a dark area. Because fayalite has high Fe and low Mg contents, fayalite appears dark in (a) and bright in (b). (c) A NanoSIMS beam spot in fayalite is indicated by arrows.

$^{55}\text{Mn}/^{52}\text{Cr}$  ratios of San Carlos olivine by SIMS and those by LA-ICP-MS (Laser Ablation-ICP-MS; an Element-XR by Thermo Fisher Scientific at NASA Johnson Space Center). The RSF and IMF values are 1.49–1.56 and 1.01–1.02 for session 2, and 1.46–1.87 and 1.00–1.01 for session 3.

Finally, we calculated the slope and intercept of isochrons of fayalite, olivine and pyroxene in each clast or meteorite based on  $^{53}\text{Cr}/^{52}\text{Cr}$ ,  $(^{53}\text{Cr}/^{52}\text{Cr})_{\text{error}}$ ,  $^{55}\text{Mn}/^{52}\text{Cr}$  and  $(^{55}\text{Mn}/^{52}\text{Cr})_{\text{error}}$  by using the York fit program ‘Isoplot 3.41’.

#### 2.4. Thermodynamic calculations

The physical–chemical formation conditions of the analyzed fayalites were evaluated through calculations of thermochemical equilibria in a closed water–rock–gas system: O–H–Mg–Fe–Ca–Si–Al–C–P–S–Cr–Na–K–Cl–Mn–Co–Ni. The framework of our thermodynamic model calculations and data sources are described in detail in Zolotov et al. (2006) and Jogo et al. (2009). The equilibria were calculated for ranges of temperature (0–350 °C), pressure (1–300 bar) and water/rock mass ratios (0.01–1) that correspond to fayalite formation conditions obtained by Zolotov et al. (2006). The system includes 123 one-component minerals, 21 mineral–solid solutions, a non-ideal gas ( $\text{H}_2\text{O}$ ,  $\text{H}_2$ ,  $\text{CO}_2$ ,  $\text{CO}$ ,  $\text{H}_2\text{S}$ ) and a non-ideal aqueous solution (98 species). Formation of  $\text{CH}_4$  was suppressed due to the inhibition of its formation at low temperatures. We used the bulk (water-free) composition of the Bali CV3<sub>OxB</sub> chondrite (Jarosewich, 1990) to represent the initial rock because we focused on CV3<sub>OxB</sub> clasts and chondrites in this study. The thermodynamic model output data include amounts and compositions of solid, gas, and aqueous phases. The calculations were performed with the GEOCHEQ code that considers non-ideal gas, aqueous, and solid solutions (Mironenko et al., 2008).

#### 2.5. Thermal modeling

It is still not known how many CV3 chondrite parent bodies existed, and their sizes and internal structures are poorly constrained. The three subgroups of CV3 chondrites experienced different styles and degrees of aqueous/metamorphic alteration and thermal metamorphism (Krot et al., 1995, 1998, 2004). This makes it difficult to discern whether

these subgroups originated from a single body or multiple bodies. In addition, metamorphic materials such as CK4-6 chondrites, metamorphic clasts in CV3 chondrites and CV meta-chondrites (NWA 3133 and NWA 1839) have mineralogical, chemical and isotopic similarities with CV3 chondrites (Irving et al., 2004; Schoenbeck et al., 2006; Greenwood et al., 2010; Jogo et al., 2013; Wasson et al., 2013; Chaumard et al., 2014). It is conceivable that such materials originated from the deep interior of the CV3 parent body. Moreover, magnetic studies of CV3 chondrites may suggest that the parent body underwent melting, igneous differentiation and Fe–Ni core formation (Carporzen et al., 2011; Elkins-Tanton et al., 2011).

There are several potential problems with the models predicting high degree thermal metamorphism inside the CV3 parent body. These include the lack of CK, CV meta-chondrites and Fe–Ni core-like materials in CV3 chondrite breccias, and differences in the bulk  $\epsilon^{54}\text{Cr}$  values of CV meta-chondrites and CV3 chondrites (e.g., Greenwood et al., 2010; Shukolyukov et al., 2011; this study). In contrast, many CV3 brecciated chondrites show mixed lithologies of different CV3 subgroups (Krot et al., 2000; Tomeoka and Tanimura, 2000; Jogo et al., 2009). This may be more consistent with an origin on a single heterogeneously altered CV3 parent body (e.g., Krot et al., 2000). In addition, unidirectional paleomagnetic directions of CV3 chondrites might be explained by shock metamorphism rather than by a dynamo within the CV3 parent body (Bland et al., 2014; Chaumard and Devouard, 2016).

In our model simulations, we derived constraints on the CV3 chondrite accretion timing and thermal history with the assumption that all three CV3 subgroups originated from a single parent body. The maximum internal temperature reached by the CV-like asteroids was determined mainly by their sizes and formation timescales. Early-formed asteroids incorporated greater amounts of short-lived nuclides and therefore experienced higher degrees of internal heating due to their decay energy, especially from  $^{26}\text{Al}$ . The CV3<sub>OxA</sub> chondrites show equilibration temperatures of about 530–590 °C, which is higher than in CV3<sub>Red</sub> and CV3<sub>OxB</sub> chondrites (Busemann et al., 2007). In our model simulations, we assumed that the peak temperatures reached by the CV asteroid is 500–600 °C. In addition, the timing of aqueous alteration provides an important

constraint on the accretion timing of the CV3 parent body because the heat generated by aqueous alteration also contributed to heating of the body. In order to obtain plausible accretion timing of the CV3 body, we calculated the accretion timing which fulfills the timing of aqueous alteration estimated from the formation age of CV3 A881317 fayalite ( $4.2_{-0.7}^{+0.8}$  Ma after CAI formation, Doyle et al., 2015). We ran models for bodies with radii of 30, 50, 100, and 200 km.

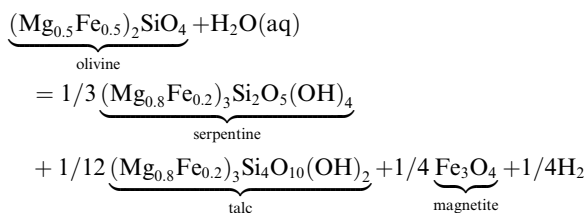
We considered a spherically-symmetric, instantaneously accreting bodies. A heat-conduction equation was solved numerically using a finite difference method and an explicit method of integral evaluation (Wakita and Sekiya, 2011):

$$\rho c \frac{\partial T}{\partial t} = \frac{1}{r^2} \frac{\partial}{\partial r} \left( r^2 K \frac{\partial T}{\partial r} \right) + A \exp(-\lambda t) \quad (1)$$

where  $\rho$  is density,  $c$  is specific heat,  $T$  is temperature,  $t$  is time,  $r$  is distance from the center,  $K$  is thermal conductivity,  $A$  is initial rate of radiogenic heat generation per unit volume, and  $\lambda$  is the decay constant of  $^{26}\text{Al}$ . We assumed that  $^{26}\text{Al}$  ( $t_{1/2} = 0.72$  Ma) was the only radiogenic heat source with the initial  $^{26}\text{Al}/^{27}\text{Al}$  ratio of  $5.25 \times 10^{-5}$  that was uniformly distributed in the protoplanetary disk by the time the majority of Ca- and Al-rich inclusions (CAIs) formed (MacPherson et al., 1995; Connelly et al., 2012; Kita et al., 2012).

We assumed no fluid-flow in the model, because fluid movement is thought not to have exceeded  $\sim\text{cm}$  scales based on chemical data on carbonaceous chondrites (e.g., Keller et al., 1994; Krot et al., 1998; Bland et al., 2009; Stracke et al., 2012; MacPherson and Krot, 2014). This is consistent with our observed homogeneous distribution of secondary minerals in an individual clast (up to  $\sim 1$  mm size) in Y86009 and A881317 breccias and in the entire thin sections of MET01074 and MET00430 ( $\sim 1 \text{ cm}^2$ ). In some fayalite-bearing CV3<sub>OxB</sub> chondrites, heterogeneous aqueous alteration ( $\sim\text{mm}$  scale) has been inferred from mineralogical observations (Keller et al., 1994). In addition, Bland et al. (2009) reported that permeability of initial chondritic materials is very low, suggesting that there was not much water flow in carbonaceous chondrite parent bodies. Thus, models of the CV parent body without fluid flow could be justified.

We assumed that hydration and oxidation reactions occurred at 0 °C, soon after the melting of ice. We assumed the initial (unaltered) rocks in the CV3 body contain elements with the atomic ratio Si:Fe:Mg = 1:1:1, which is consistent with the approximate ratios of the solar abundance (Lodders, 2003) and close to bulk chemical compositions of CV3 chondrites; the original mineralogy was assumed to be olivine,  $(\text{Mg}_{0.5}\text{Fe}_{0.5})_2\text{SiO}_4$  (Hutchison, 2007; Wakita and Sekiya, 2011). The simplified hydration-oxidation reaction is represented as follows:



This reaction has an enthalpy of  $2.77 \times 10^5$  kJ/kg, as calculated from enthalpies of compounds at 25 °C (Holland and Powell, 1998). We assumed the reaction enthalpy is the same at 0 and 25 °C. We also assumed the following initial constants for the CV parent body: temperature of  $-123$  °C (corresponds to 3–4 AU in the protoplanetary disk); Al content of 1.75 wt% (Hutchison, 2007), water/rock mass ratio of 0.1 (fayalite formation conditions in CV3<sub>OxB</sub> Bali chondrites; Zolotov et al., 2006). Physical properties and other details of modeling are shown in Wakita and Sekiya (2011).

### 3. RESULTS

#### 3.1. Fayalite occurrences

Petrographic observations indicate that Y86009 and A881317 are breccias consisting of many clasts (Fig. 2). A typical clast (from  $\sim 0.5$  to  $\sim 1$  mm in size) is composed of chondrules and surrounding olivine-rich fine-grained ( $< 100 \mu\text{m}$  in thickness) materials (Fig. 2c and d). Clasts are either embedded in the host meteorite matrix or are in direct contact with adjacent clasts. Secondary minerals such as fayalite, ferroan olivine, magnetite, troilite and high-Ca pyroxene occur in chondrules, host matrix and fine-grained materials. The distribution of secondary minerals differs between the clasts. These mineralogical settings are similar to other CV3 chondrite breccias containing fayalite (Krot et al., 1995, 2000; Tomeoka and Tanimura, 2000; Jogo et al., 2009; Tomeoka and Ohnishi, 2010, 2014; Brearley and Krot, 2013). In contrast, MET00430 and MET01074 appear to be unbrecciated. The major secondary minerals in these chondrites are similar to those in Y86009 and A881317, and other fayalite-bearing CV3 chondrites.

In both brecciated and non-brecciated meteorites, fayalite occurs in the interiors and the peripheries of chondrules, in fine-grained materials in clasts, and in the host matrix (Fig. 2). Fayalite grains with 5–50  $\mu\text{m}$  in size occur as isolated crystals and constituents of veins, and commonly coexists with troilite and/or magnetite. The composition of the fayalite is typically from  $\text{Fa}_{100}$  to  $\text{Fa}_{80}$ , occasionally down to  $\text{Fa}_{\sim 60}$  (Table 1). Almost all fayalite grains reveal Fe–Mg zoning (the zoning scale is up to 5  $\mu\text{m}$ ), where the Fa# decreases toward at the rim. Such occurrences are consistent with those observed in CV3 fayalite (Hua and Buseck, 1995; Krot et al., 1995, 1998, 2000; Hutcheon et al., 1998; Choi et al., 2000; Hua et al., 2005; Jogo et al., 2009). We defined such fayalite and ferroan olivine with  $\text{Fa}_{60-100}$  as “fayalite” in this paper. Petrologic observations of fayalite grains that used for Mn–Cr isotopic dating are summarized in Table 1.

EPMA analysis shows similar fayalite compositions in the same clasts or within non-brecciated chondrites (Table 1). For example, in the MET01074, fayalite shows similar compositional trends:  $\text{Fa}_{\sim 100}$  at the center and  $\text{Fa}_{80-90}$  at the rim of a single fayalite crystal. In the Y86009 and A881317 breccias, Fa# is similar in the same clast but it differs between clasts. Such occurrences were also observed in Vigarano CV3 breccia (Jogo et al., 2009).

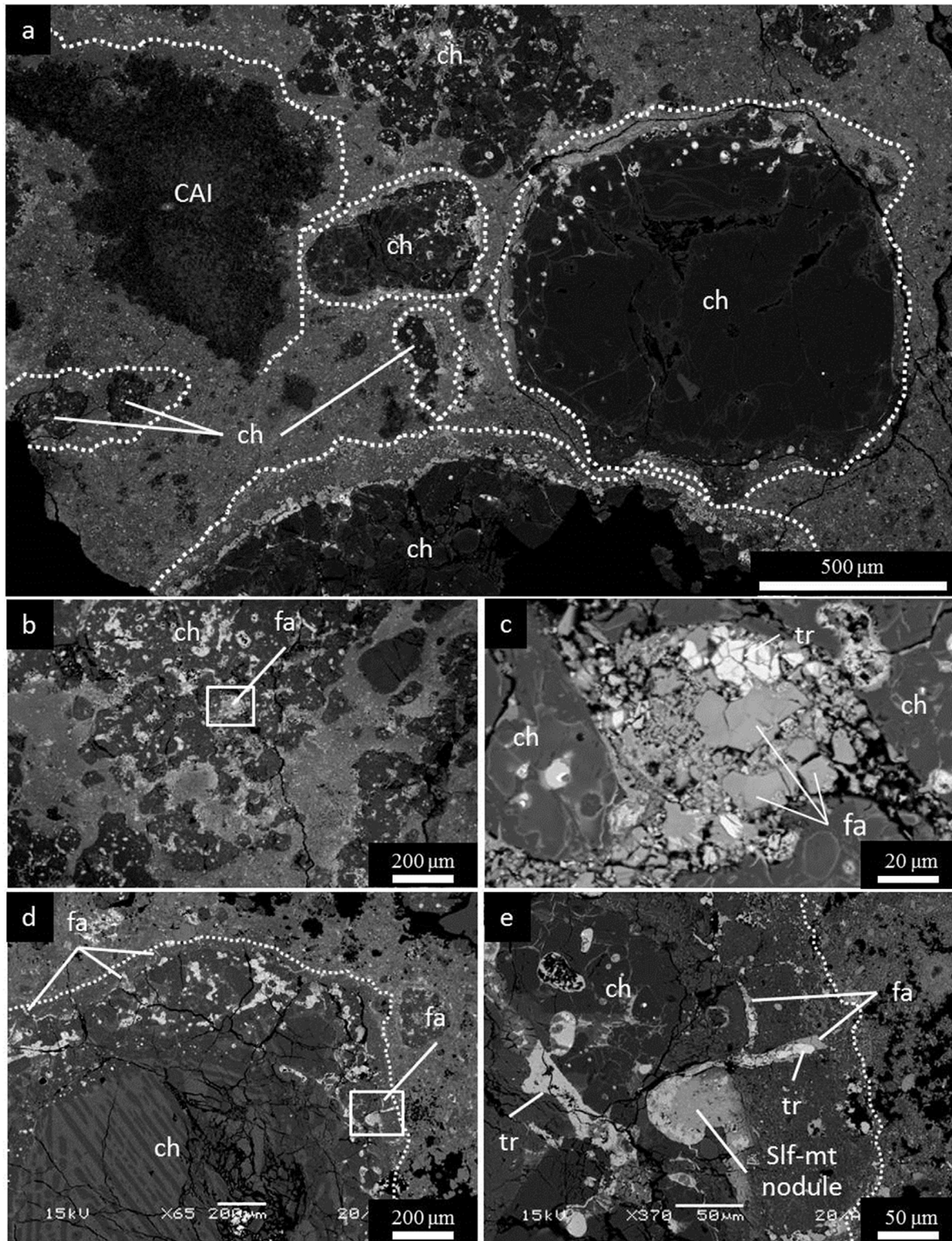


Fig. 2. Back scattered electron (BSE) images of CV3 A881317 (a–c) and Y86009 (d and e). (a) A representative brecciated nature of A881317. Clasts consisting of chondrule (ch) or CAI and surrounding olivine-rich fine-grained materials are either embedded in host matrix or are in direct contact with adjacent clasts. (b) Fayalite (fa) grains occur inside a chondrule. (c) Magnified view of region in b. Fayalite grains coexists with troilite (tr). (d) Fayalite-bearing veins occur around a chondrule. (e) Magnified view of region in d. Veins consisting of fayalite and troilite extend from a sulfide (slf) – magnetite (mt) nodule at the chondrule surface into surrounding olivine-rich fine-grained materials. Clast boundaries are indicated by dotted lines in a, d and e.

Table 1  
Summary of petrologic observations of fayalite.

| Meteorite | Clast          | Grain                  |       |
|-----------|----------------|------------------------|-------|
|           |                | Size ( $\mu\text{m}$ ) | Fa#   |
| A881317   | 1              | 30 $\times$ 30         | 98    |
|           | 3              | 20 $\times$ 20         | 99    |
|           | 4              | 20 $\times$ 20         | 79    |
|           | 6              | 10 $\times$ 15         | 97    |
| Y86009    | 1              | 30 $\times$ 30         | 99    |
|           |                | 30 $\times$ 30         | 100   |
|           |                | 20 $\times$ 20         | 99    |
|           |                | 50 $\times$ 30         | 99    |
|           |                | 10 $\times$ 10         | 97–83 |
|           | 2              | 10 $\times$ 10         | 96–86 |
|           | 4              | 10 $\times$ 20         | 100   |
|           | 7              | 10 $\times$ 10         | 96–87 |
|           | 8              | 10 $\times$ 20         | 98–95 |
|           | 9              | 10 $\times$ 10         |       |
|           | 14             | 10 $\times$ 20         |       |
| Host rock | 10 $\times$ 20 | 97–79                  |       |
|           | 10 $\times$ 20 | 85–70                  |       |
| MET00430  | Host rock      | 15 $\times$ 25         | 82–60 |
|           |                | 10 $\times$ 20         | 92–62 |
|           |                | 10 $\times$ 10         | 79–65 |
| MET01074  | Host rock      | 20 $\times$ 30         | 97–82 |
|           |                | 5 $\times$ 20          |       |
|           |                | 20 $\times$ 25         | 99–91 |

### 3.2. Mn–Cr systematics of fayalite

Mn–Cr systematics was measured in 27 fayalite grains in Y86009, A881317, MET01074 and MET00430 (Table 2, Fig. 3). Measurements were performed in three sessions using two SIMS instruments: [session 1] clast 1 in Y86009 by ims-6f SIMS, [session 2] clasts 2, 4, 7, 8, 9, 14 and host in Y86009 by NanoSIMS 50L and [session 3] clasts 1, 3, 4 and 6 in A881317, and non-brecciated MET01074 and MET00430 by NanoSIMS 50L. Recently, compositional and analytical dependence of the  $^{55}\text{Mn}/^{52}\text{Cr}$  RSFs have been reported in several studies (e.g., Sugiura et al., 2005; McKibbin et al., 2013; Doyle et al., 2015), suggesting that it would be improper to compare the inferred  $^{53}\text{Mn}/^{55}\text{Mn}$  ratios of fayalite obtained with different analytical conditions or standard minerals. This means that we can only compare the obtained Mn–Cr data from the same session but should carefully consider those from different sessions or the literature data.

Multiple fayalite grains in Y86009 clast 1, non-brecciated MET01074 and MET00430 were measured in sessions 1, 3 and 3, respectively (hereafter we define the non-brecciated chondrite as a large “clast”; i.e., non-brecciated MET01074 and MET00430 could be considered as a single clast). Because all data in individual clasts were obtained during the same session, we can simply compare these Mn–Cr data in each clast. Regardless of various Fa# of measured fayalite (Table 2), the data points lie within analytical errors on a straight line (Fig. 3a, d, e). Inferred initial  $^{53}\text{Mn}/^{55}\text{Mn}$  ratios ( $2\sigma$ ) are  $(1.9 \pm 0.4) \times 10^{-6}$  for fayalite in clast 1 in Y86009,  $(1.6 \pm 0.8) \times 10^{-6}$

for those in MET01074, and  $(1.4 \pm 0.5) \times 10^{-6}$  for those in MET00430 (Fig. 4). These results suggest that formation of fayalite with different Fa# occurred within a period of about 2–6 million years within each clast. The duration of the alteration event is constrained by the error in the isochron but could be much shorter.

Fayalite grains in six different clasts (clasts 2, 4, 7, 8, 9 and 14) and host in Y86009, and four different clasts (clasts 1, 3, 4 and 6) in A881317 were measured in sessions 2 and 3, respectively. As all data in each chondrite were obtained in the same session, simple comparison of the obtained Mn–Cr data would be possible. The Mn–Cr data points all spread along a single line in each chondrite (Fig. 3b, c), suggesting that fayalite formation in different clasts may have occurred during the same alteration episode at the same time in each chondrite. The inferred initial  $^{53}\text{Mn}/^{55}\text{Mn}$  ratios ( $2\sigma$ ) are  $(1.6 \pm 0.3) \times 10^{-6}$  for the six clasts and host in Y86009, and  $(1.9 \pm 0.8) \times 10^{-6}$  for the four clasts in A881317 (Fig. 4).

Fayalite in A881317, MET01074 and MET00430 were measured in the same session 3, therefore, the inferred initial  $^{53}\text{Mn}/^{55}\text{Mn}$  ratios in fayalite from these three chondrites can be compared. The inferred initial  $^{53}\text{Mn}/^{55}\text{Mn}$  ratios are identical within errors (Fig. 4), suggesting that fayalite may have formed at approximately the same time in each chondrite. These ratios also agree with those from clast 1 in Y86009 [session 1], six clasts and host in Y86009 [session 2], Mokoia (Hutcheon et al., 1998), Kaba (Hua et al., 2005) and Vigarano (Jogo et al., 2009) (Fig. 4). As all data mentioned here were corrected by  $^{55}\text{Mn}/^{52}\text{Cr}$  RSFs of San Carlos olivine, not fayalite, the obtained ages could include potential errors. As the sequence of timing for fayalite formation may not be changed, all fayalite in these CV3 chondrites might have formed at the same period. In order to confirm this implication, Mn–Cr measurements on fayalite in these chondrites by using fayalite standards are needed.

### 3.3. Thermodynamic conditions of fayalite formation and thermal evolution models for the CV3 chondrite parent body

We estimated fluid pressure and temperature during the formation of fayalite in CV3<sub>OXB</sub> chondrites. Zolotov et al. (2006) found that fayalite (Fa<sub>100-88</sub>) forms only over a narrow range of water/rock mass ratios ( $\sim 0.1$ – $0.15$ ), temperature and pressures (Fig. 5); fayalite with higher Fa# formed at lower fluid pressures and temperatures. For olivine compositions Fa<sub>88-10</sub>, such correlations were not obtained; formation conditions for these olivines are  $>100$  °C and  $>10$  bars, and do not depend on Fa# (Zolotov et al., 2006).

Our thermal evolutionary models of the CV3 chondrite parent body constrain the timescales of its accretion and aqueous alteration. For peak core temperatures of 500–600 °C, our models show that this body accreted between 3.0 and 3.3 Ma after CAI formation (Fig. 6). These accretion ages correspond to initial  $^{26}\text{Al}/^{27}\text{Al}$  ratios of CV3 materials between  $2.2 \times 10^{-6}$  and  $2.9 \times 10^{-6}$ . The decay of  $^{26}\text{Al}$  gradually heated the CV3 parent body, reaching 0 °C and melting ice about 0.3–0.4 Ma after initial accretion. The melting of ice led to rapid warming due to

Table 2

Mn–Cr isotopic data of fayalite. Listed errors are two standard deviation for  $^{55}\text{Mn}/^{52}\text{Cr}$  and two standard deviation of the mean for  $^{53}\text{Cr}/^{52}\text{Cr}$ . Fa# of the SIMS measurement spots are shown.

| Sample   | Clast      | SIMS         | Session      | Spot#      | Fa#         | $^{55}\text{Mn}/^{52}\text{Cr}$ | $2\sigma$ | $^{53}\text{Cr}/^{52}\text{Cr}$ | $2\sigma_m$ |          |
|----------|------------|--------------|--------------|------------|-------------|---------------------------------|-----------|---------------------------------|-------------|----------|
| A881317  | 1          | NanoSIMS 50L | 3            | FA A88 1-1 | 98          | 9.43E+04                        | 1.00E+04  | 2.49E–01                        | 2.10E–02    |          |
|          |            |              |              | OL A88 1-1 |             | 6.80E+00                        | 6.48E–01  | 1.15E–01                        | 1.38E–04    |          |
|          | 3          | NanoSIMS 50L |              | FA A88 3-1 | 99          | 4.19E+05                        | 2.23E+04  | 9.41E–01                        | 6.02E–02    |          |
|          | 4          | NanoSIMS 50L |              | FA A88 4-1 | 79          | 2.64E+04                        | 6.92E+03  | 1.67E–01                        | 2.09E–02    |          |
|          | 6          | NanoSIMS 50L |              | FA A88 6-1 | 97          | 6.60E+04                        | 1.80E+04  | 2.58E–01                        | 1.96E–02    |          |
| Y86009   | 1          | ims-6f       | 1            | FA Y86 1-1 | 100         | 1.26E+04                        | 8.84E+02  | 1.33E–01                        | 1.52E–02    |          |
|          |            |              |              | FA Y86 1-2 | 100         | 2.23E+04                        | 1.41E+03  | 1.58E–01                        | 1.71E–02    |          |
|          |            |              |              | FA Y86 1-3 | 100         | 1.51E+04                        | 3.13E+03  | 1.37E–01                        | 1.70E–02    |          |
|          |            |              |              | FA Y86 1-4 | 100         | 5.61E+04                        | 1.18E+04  | 2.60E–01                        | 4.98E–02    |          |
|          |            |              |              | FA Y86 1-5 | 100         | 1.24E+04                        | 1.39E+03  | 1.30E–01                        | 1.48E–02    |          |
|          |            |              |              | FA Y86 1-6 | 99          | 9.01E+03                        | 3.93E+03  | 1.15E–01                        | 2.14E–02    |          |
|          |            |              |              | FA Y86 1-7 | 99          | 2.11E+04                        | 4.10E+03  | 1.79E–01                        | 3.78E–02    |          |
|          |            |              |              | OL Y86 1-2 |             | 3.21E–01                        | 1.75E–02  | 1.14E–01                        | 1.04E–03    |          |
|          |            |              |              | OL Y86 1-3 |             | 3.35E–01                        | 2.24E–02  | 1.14E–01                        | 3.75E–03    |          |
|          |            |              |              |            | 2           | NanoSIMS 50L                    | 2         | FA Y86 2-1                      | 97          | 2.65E+04 |
|          |            | 4            | NanoSIMS 50L | 2          | FA Y86 4-1  | 96                              | 1.06E+03  | 3.04E+02                        | 1.16E–01    | 1.12E–03 |
|          |            | 7            | NanoSIMS 50L | 2          | FA Y86 7-1  | 100                             | 1.27E+05  | 2.91E+04                        | 3.44E–01    | 1.74E–02 |
|          | FA Y86 7-2 |              |              |            | 100         | 5.91E+04                        | 1.14E+04  | 2.18E–01                        | 1.42E–02    |          |
|          |            | 8            | NanoSIMS 50L | 2          | FA Y86 8-1  | 96                              | 2.59E+04  | 3.28E+03                        | 1.57E–01    | 4.72E–03 |
|          |            | 9            | NanoSIMS 50L | 2          | PX Y86 8-1  |                                 | 4.63E–01  | 3.66E–02                        | 1.14E–01    | 2.39E–04 |
|          |            |              |              |            | FA Y86 9-1  | 98                              | 7.16E+04  | 1.99E+04                        | 2.31E–01    | 1.67E–02 |
|          |            | 9            | NanoSIMS 50L | 2          | FA Y86 9-2  | 98                              | 6.35E+02  | 1.60E+02                        | 1.16E–01    | 1.94E–03 |
|          |            |              |              |            | FA Y86 9-3  | 98                              | 5.12E+03  | 7.11E+02                        | 1.20E–01    | 2.34E–03 |
|          |            |              |              |            | OL Y86 9-1  |                                 | 9.41E–01  | 6.39E–02                        | 1.13E–01    | 3.51E–04 |
|          |            | 14           | NanoSIMS 50L | 2          | FA Y86 14-1 |                                 | 5.89E+03  | 1.95E+03                        | 1.22E–01    | 2.98E–03 |
|          | Host rock  | NanoSIMS 50L | 2            | FA Y86 H-1 | 97          | 2.53E+03                        | 3.32E+02  | 1.17E–01                        | 2.15E–03    |          |
|          |            |              |              | PX Y86 H-1 |             | 2.05E–01                        | 2.09E–02  | 1.14E–01                        | 4.42E–04    |          |
| MET00430 | Host rock  | NanoSIMS 50L | 3            | FA MET00-1 | 82          | 2.73E+03                        | 3.89E+02  | 1.17E–01                        | 9.84E–04    |          |
|          |            |              |              | FA MET00-2 | 92          | 1.12E+04                        | 2.22E+03  | 1.29E–01                        | 2.56E–03    |          |
|          |            |              |              | FA MET00-3 | 79          | 8.00E+03                        | 1.13E+03  | 1.26E–01                        | 1.29E–03    |          |
|          |            |              |              | OL MET00-1 |             | 9.04E–01                        | 6.09E–02  | 1.13E–01                        | 5.18E–04    |          |
|          |            |              |              | PX MET00-1 |             | 3.07E–01                        | 2.11E–02  | 1.14E–01                        | 5.21E–04    |          |
| MET01074 | Host rock  | NanoSIMS 50L | 3            | FA MET01-1 | 97          | 5.63E+03                        | 3.78E+02  | 1.27E–01                        | 1.08E–03    |          |
|          |            |              |              | FA MET01-2 |             | 5.51E+04                        | 7.25E+03  | 2.22E–01                        | 4.15E–03    |          |
|          |            |              |              | FA MET01-3 | 99          | 3.98E+04                        | 6.29E+03  | 1.56E–01                        | 1.60E–02    |          |
|          |            |              |              | FA MET01-4 |             | 1.53E+05                        | 4.21E+04  | 2.91E–01                        | 3.00E–02    |          |
|          |            |              |              | FA MET01-6 | 97          | 1.87E+05                        | 1.32E+04  | 2.87E–01                        | 1.85E–02    |          |
|          |            |              |              | OL MET01-1 |             | 5.53E–01                        | 5.77E–02  | 1.14E–01                        | 3.09E–04    |          |
|          |            |              |              | PX MET01-1 |             | 7.00E–01                        | 5.40E–02  | 1.13E–01                        | 3.02E–04    |          |

exothermic hydration of olivine to phyllosilicates such as serpentine. Aqueous alteration began almost simultaneously (within 0.1 Ma) throughout the CV3 parent body (Fig. 7). After aqueous alteration ceased, the decay of  $^{26}\text{Al}$  continued to raise the internal temperature. When heat loss by radiation exceeded the decay heat of  $^{26}\text{Al}$ , the temperature of the body started to decrease. Smaller sized bodies began cooling at earlier times.

Fig. 8 shows the peak temperature and timing of aqueous alteration as a function of accretion ages of the CV3 chondrite parent body having a radius of 50 km. The accretion timing which fulfills the formation age of CV3 A881317 fayalite ( $4.2_{-0.7}^{+0.8}$  Ma after CAI formation, Doyle et al., 2015) is  $\sim 3.2$ – $4.0$  Ma after CAI formation. In the body with such accretion ages, peak temperature reached  $\sim 320$ – $540$  °C.

## 4. DISCUSSION

### 4.1. Conditions and timing of fayalite formation

At an early stage of thermal evolution of the CV3 chondrite parent body, the temperature increased and passed through the stability field of fayalite (Figs. 5 and 7b). Fayalite grains with high Fa# formed early at low temperature. These high Fa# fayalites were subsequently overgrown by low Fa# fayalite that formed at higher temperatures (arrows in Fig. 5). This formation sequence led to the Fe–Mg zoning pattern observed in fayalite in CV3 chondrites (Table 1) as proposed by Zolotov et al. (2006) and Jogo et al. (2009). The Fe–Mg zoning pattern in fayalite is a signature of the formation process and is not related to postcrystallization Fe–Mg interdiffusion. In order to form

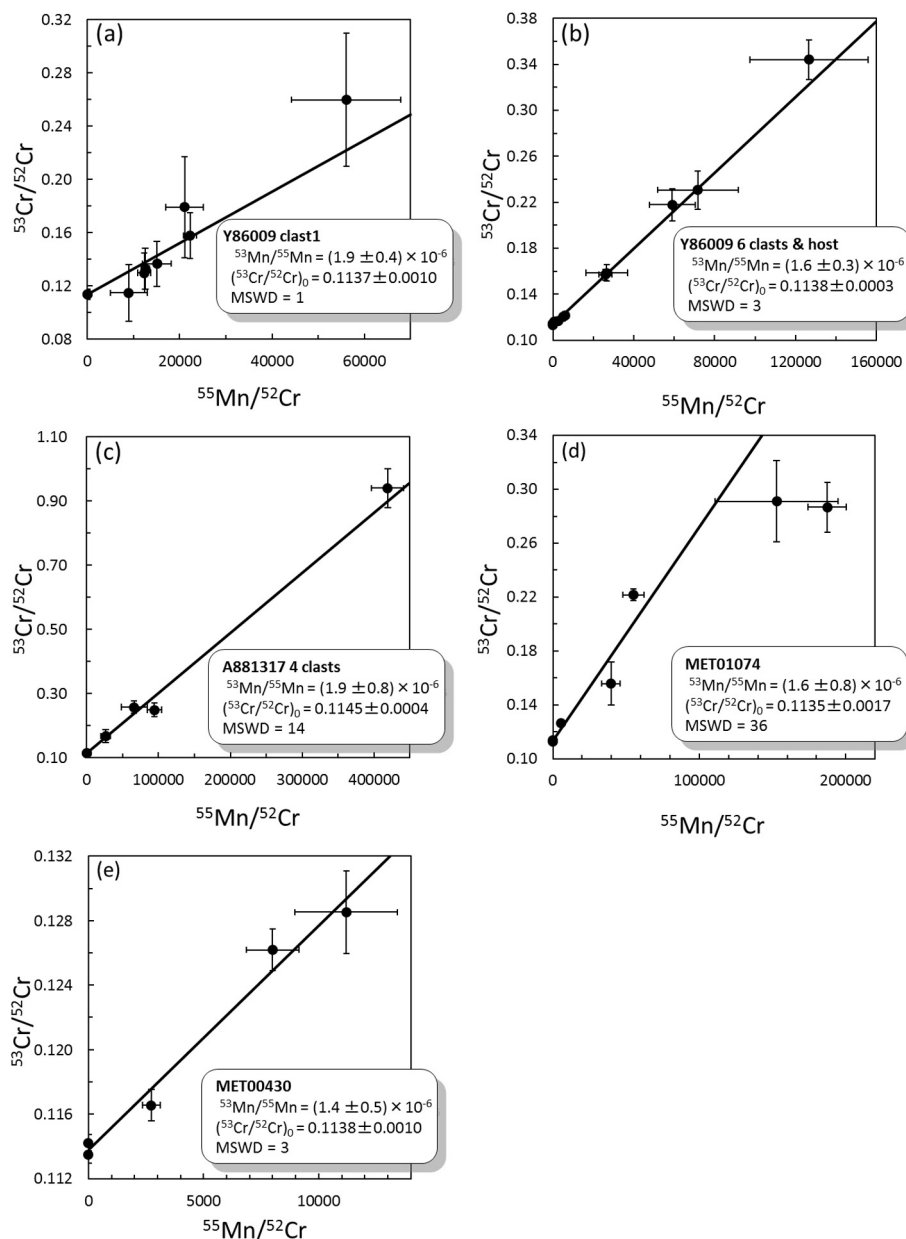


Fig. 3. Mn–Cr evolutionary diagrams for fayalite in clast 1 from Y86009 (a), six clasts and host chondrites from Y86009 (b), four clasts from A881317 (c), host chondrites from MET01074 (d), and MET00430 (e). Error bars are  $2\sigma$ .

the observed Fe–Mg zoning scale (up to  $5 \mu\text{m}$ ) by diffusion at  $400 \text{ }^\circ\text{C}$  (peak metamorphic temperature of CV3<sub>OXB</sub> chondrites containing fayalite; Busemann et al., 2007), 50 Ma is required (Fe–Mg diffusion coefficient at  $400 \text{ }^\circ\text{C}$  is about  $10^{-26} \text{ m}^2/\text{s}$ ; Chakraborty et al., 1994; Chakraborty, 1997). This diffusion duration is longer than the estimated time-scale of CV3 parent body thermal metamorphism ( $<10 \text{ Ma}$ ; e.g., Young, 2001), suggesting that the observed Fe–Mg zoning of fayalite did not result from the thermal metamorphism. After formation of fayalite, clasts containing fayalite were incorporated into their host meteorites, and thus fayalite in each clast retained distinct Fa# trends.

Fe and Mg inter-diffusion coefficients in olivine are higher than Cr and Mn diffusivities in olivine under  $f\text{O}_2$  and temperature conditions of fayalite-bearing CV3<sub>OXB</sub> chondrites (Buening and Buseck, 1973; Morioka, 1981; Chakraborty, 1997; Ito and Ganguly, 2006; Busemann et al., 2007; Righter and Neff, 2007). Because Fe–Mg diffusive exchange did not occur between fayalite and surrounding phases, Cr and Mn should not have been disturbed by diffusion processes since their formation. Therefore, the obtained Mn–Cr ages of fayalite represent the timing when fayalite started to form during aqueous alteration in their parent asteroids, not the timing of thermal metamorphism.

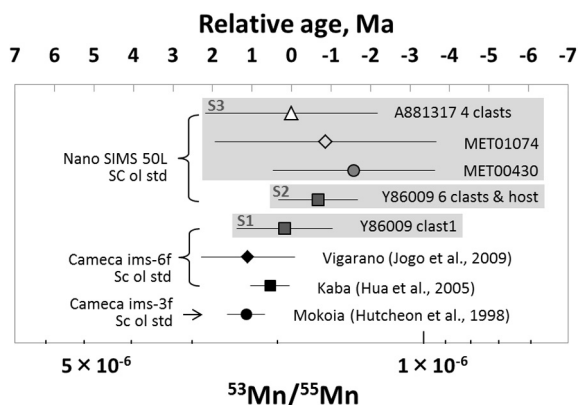


Fig. 4. The initial  $^{53}\text{Mn}/^{55}\text{Mn}$  ratios of CV3 fayalite whose  $^{55}\text{Mn}/^{52}\text{Cr}$  ratios were corrected by RSFs of San Carlos olivine standard (SC of std). Age differences are calculated relative to mean initial  $^{53}\text{Mn}/^{55}\text{Mn}$  ratios of fayalite in A881317 (i.e., initial  $^{53}\text{Mn}/^{55}\text{Mn}$  ratio of  $1.9 \times 10^{-6}$ ). Error bars are  $2\sigma$ . Fayalite in the clast 1 in Y86009 were measured in [session 1 (S1)] with Cameca ims-6f, those in six clasts and host in Y86009 were measured in [session 2 (S2)] with NanoSIMS 50L and those in four clasts in A881317, MET01074 and MET00430 were measured in [session 3 (S3)] with NanoSIMS 50L. Initial  $^{53}\text{Mn}/^{55}\text{Mn}$  ratios of fayalite in Mokoia (Hutcheon et al., 1998, Cameca ims-3f), Kaba (Hua et al., 2005, Cameca ims-6f) and Vigarano (Jogo et al., 2009, Cameca ims-6f) are also shown for reference.

#### 4.2. Accretion time of the CV3 chondrite parent body containing fayalite

Our thermal evolutionary models yield constraints on the accretion time of the CV3 chondrite parent body from the timing of aqueous alteration. The thermal evolution model and Mn–Cr measurements of fayalite both indicate that aqueous alteration occurred over a brief time interval in the CV3 parent body. In order to be consistent with the measured fayalite formation ages and estimated peak metamorphic temperature of the CV parent body, the thermal evolutionary model constrains the accretion timescale of the CV3 chondrite parent body to be 3.2–3.3 Ma after CAI formation (Fig. 9).

According to radial diffusion model of turbulent disk, solid materials within the main asteroidal belt (2–4 AU) would be fully mixed after 1 Ma (Cuzzi et al., 2010). In order to preserve group-specific chemical and isotopic characters of chondrules, the parent body of each chondrite group should have accreted within 1 Ma of chondrule formation. Chondrules in CV3 chondrites often show disturbed Al–Mg systematics due to alteration in the CV3 parent body (e.g., Hutcheon et al., 2009; Kita and Ushikubo, 2012). Measurements of Al–Mg formation ages of the least altered chondrules in CV3 chondrites have yielded initial  $^{26}\text{Al}/^{27}\text{Al}$  ratios of  $(\sim 2\text{--}6) \times 10^{-6}$  corresponding to  $\sim 2.0\text{--}3.4$  Ma after CV3 CAI formation (Mishra and Chaussidon, 2014; Nagashima et al., 2015). In order to be consistent with the radial diffusion model, CV3 chondrite parent body should have accreted at about  $<3.0\text{--}4.4$  Ma after CAI formation (Fig. 9). This timing is

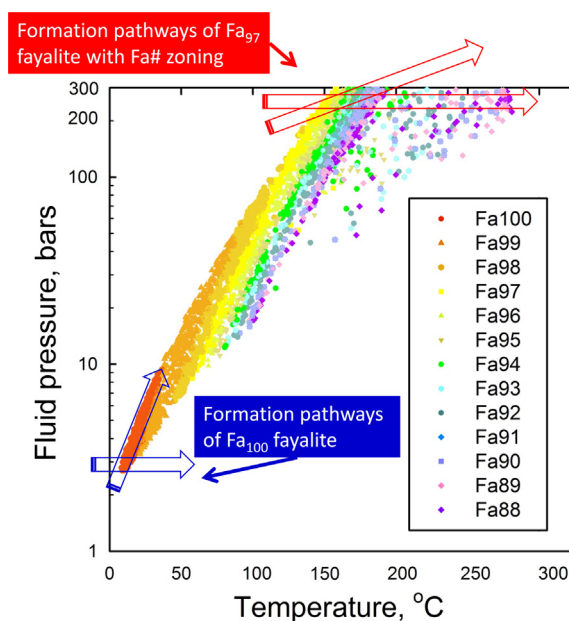


Fig. 5. Temperature and fluid pressure formation conditions of fayalite of  $\text{Fa}_{100-88}$  at water/rock mass ratios of 0.1–0.15. The stability field of each  $\text{Fa}\#$  is shown in different colored symbols. Fayalite with  $\text{Fa}_{100-88}$  form at fluid pressure of about 3–>300 bars and temperatures of about 30–>150 °C;  $\text{Fa}_{100}$  fayalite formed at about 3–10 bars and 10–40 °C. Lower  $\text{Fa}\#$  fayalite formed at higher fluid pressure and temperature conditions. Plausible formation pathways of fayalite with  $\text{Fa}\#$  zoning in which  $\text{Fa}_{97}$  is present at the center and  $\text{Fa}\#$  decreases toward the rim (e.g., clast 2 in the Y-86009) are shown by upper red arrows, and those of  $\text{Fa}_{100}$  fayalite without  $\text{Fa}\#$  zoning (e.g., clast 1 in the Y-86009) are indicated by blue arrows. (For interpretation of the references to colour in this figure legend, the reader is referred to the web version of this article.)

in agreement with our estimates for the accretion timing of the CV3 chondrite parent body containing fayalite.

Previous CV3 parent body thermal evolutionary models have adopted different values for the peak temperature and other initial parameters (e.g., Elkins-Tanton et al., 2011; Fu and Elkins-Tanton, 2014; Doyle et al., 2015). Elkins-Tanton et al. (2011) assumed that CV3 parent body had a molten Fe–Ni core (peak temperature of  $>1200$  °C) to explain paleomagnetic records in the CV3<sub>OxA</sub> Allende, concluding that it accreted by  $\sim 1.5$  Ma after CAI formation with  $>\sim 200$  km in radius. However, because the timing when temperature of such CV3 body reached fayalite formation conditions (i.e., 10–300 °C with increasing temperature; this study) is much earlier than the formation age of A881317 fayalite (Doyle et al., 2015), CV3<sub>OxB</sub> materials with fayalite might not have originated from such body. The estimated peak temperature of the CV3 body of  $\sim 500\text{--}540$  °C (this study) is lower than that of the CV3 body with a molten Fe–Ni core (Elkins-Tanton et al., 2011) or equilibrated temperature of CV3-like metamorphic materials such as CK4-6 chondrites (e.g., Chaumard and Devouard, 2016). This suggests that strong thermal metamorphism did not occur in the CV3 chondrite parent body where fayalite formed.

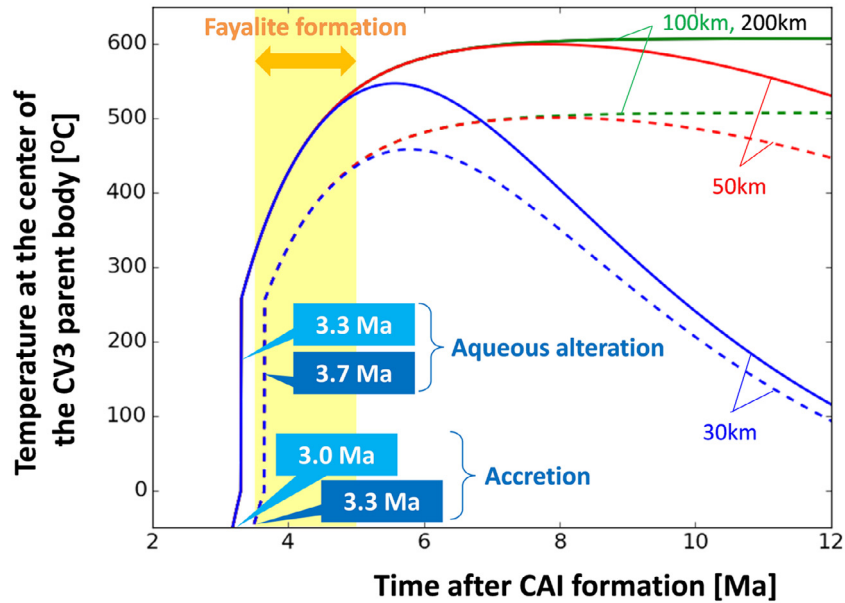


Fig. 6. Temperature evolution at the center of the CV3 parent body with radii of 30 km (blue), 50 km (red), 100 km (green), 200 km (black). The CV3 body would accrete at  $\sim 3.3$  Ma after CAI formation in order to reach the peak temperature of 500 °C (dashed lines) and at  $\sim 3.0$  Ma after CAI formation to reach 600 °C (solid lines). The pathways of temperature evolution of the body with 100 km and 200 km in radii are same in the time range of this figure. Aqueous alteration with increasing temperature occurs at about 3.3 Ma and 3.7 Ma after CAI formation in the body with peak temperature of 600 °C and 500 °C, respectively. The CV3 A881317 fayalite formation age of about  $4.2^{+0.8}_{-0.7}$  Ma after CAI formation (yellow area, Doyle et al., 2015) is identical to the aqueous alteration timing in the body with peak temperature of 500 °C but inconsistent with that of 600 °C. (For interpretation of the references to colour in this figure legend, the reader is referred to the web version of this article.)

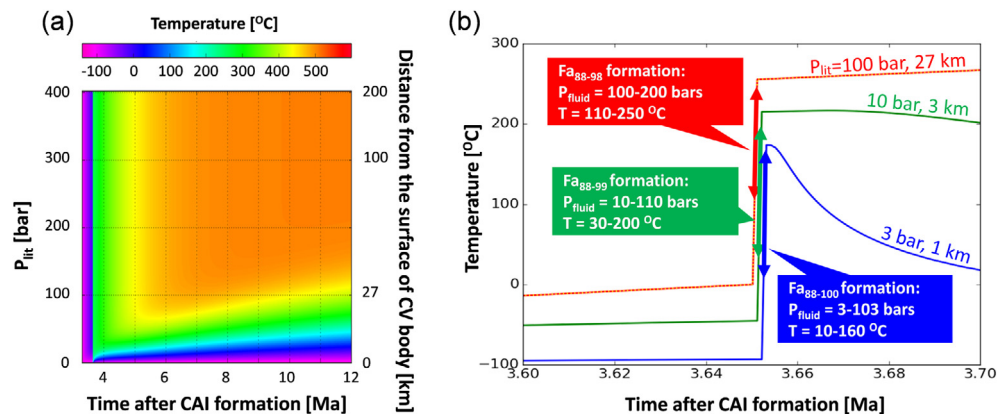


Fig. 7. Temperature-lithostatic pressure profile of the CV3 parent body with 200 km in radius that accreted at 3.3 Ma after CV3 CAIs (peak temperature of 500 °C). (a) Temperature evolution at lithostatic pressures ( $P_{lit}$ ) of the body. Temperature differences are indicated by the color scale. (b) Temperature evolution at lithostatic pressures of 3 bars (1 km distance from the surface of the body; blue), 10 bars (3 km distance from the surface; green), and 100 bar (27 km distance from the surface of the body; red) are shown.  $Fa\#$ , fluid pressure ( $P_{fluid}$ ), and temperature ranges of fayalite formation at each lithostatic pressure is shown by labels and bold arrows colored by blue ( $Fa_{88-100}$ ,  $P_{fluid} = 3-103$  bars, 10–160 °C at  $P_{lit} = 3$  bars), green ( $Fa_{88-99}$ ,  $P_{fluid} = 10-110$  bars, 30–200 °C at  $P_{lit} = 10$  bars) and red ( $Fa_{88-98}$ ,  $P_{fluid} = 100-200$ , 110–250 °C at  $P_{lit} = 100$  bars). Fayalite forms at the inner and outer parts of the body at about 3.7 Ma after CAI formation. (For interpretation of the references to colour in this figure legend, the reader is referred to the web version of this article.)

#### 4.3. Constraints on sizes of the CV3 chondrite parent body containing fayalite

The minimum size of the CV3 chondrite parent body can be constrained by the fluid pressure in which CV3 fayalite having  $Fa_{<96}$  formed. For example, in order to form

fayalite with  $Fa_{97}$  at the center and  $Fa_{83}$  at the rim (clast 2 in the Y-86009), temperature and fluid pressure need to pass through the stability field of  $Fa_{97}$  first and subsequently through that of  $Fa_{96-83}$ . Such pathways could be created if formation of  $Fa_{97}$  occurred at fluid pressure of 200–300 bars (upper arrows in Fig. 5). Many fayalite grains

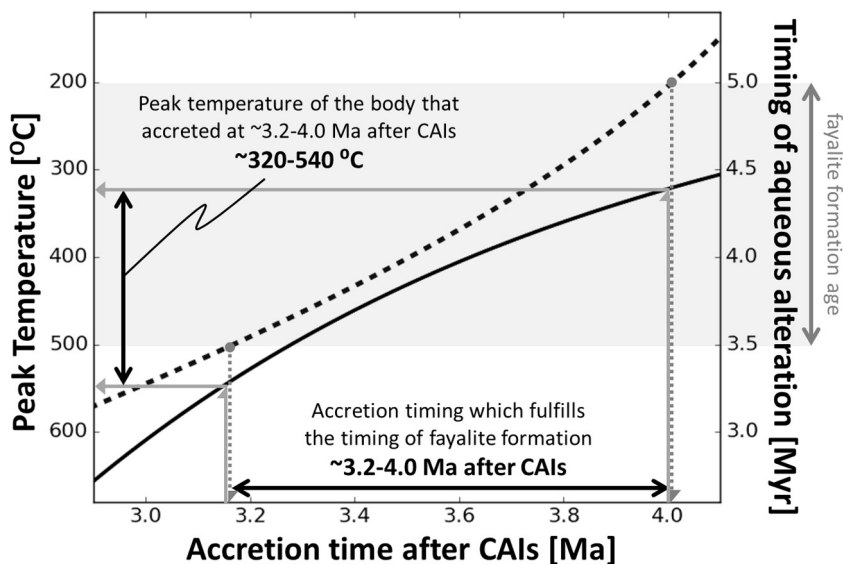


Fig. 8. Peak temperature of the body (solid line) and timing of aqueous alteration (dashed line) as a function of accretion timing of the CV3 chondrite parent body with radius of 50 km. The results are almost the same in the body with radius of 30, 100, and 200 km. The accretion timing of the CV3 parent body is  $\sim 3.2\text{--}4.0$  Ma after CAI formation based on the timing of aqueous alteration estimated from the formation age (light gray area) of CV3 A881317 fayalite (about  $4.2^{+0.8}_{-0.7}$  Ma after CAI formation, Doyle et al., 2015). Peak temperature of the body with such accretion timing is  $\sim 320\text{--}540$  °C.

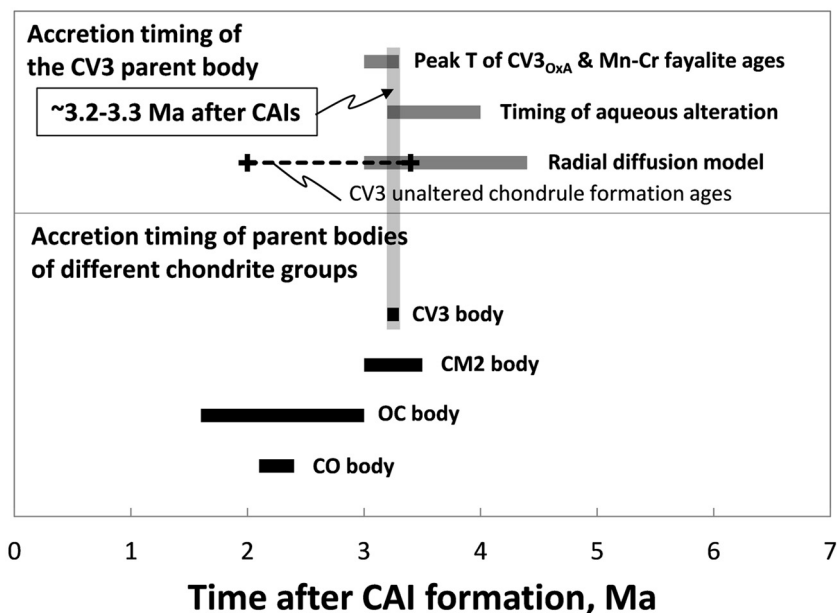


Fig. 9. Accretion timing of the CV3 chondrite parent body (upper) and its comparison with CM2, CO and ordinary (OC) chondrite parent bodies (below). The accretion timing of the CV3 parent body is constrained from different conditions: (i) about 3.0–3.3 Ma after CAI formation based on the thermal modeling of the body with peak temperature of 500–600 °C (equilibrated temperature of CV3<sub>OxA</sub> chondrites, Busemann et al., 2007) and Mn–Cr ages of fayalite (this study), (ii) about 3.2–4.0 Ma after CAI formation which satisfies the timing of aqueous alteration estimated from thermal modeling and the absolute formation age of CV3 A881317 fayalite (Doyle et al., 2015) and (iii) about <3.0–4.4 Ma after CAI formation from radial diffusion model (Cuzzi et al., 2010) requiring <1 Ma accretion of the CV3 body after CV3 chondrule formation of about 2.0–3.4 Ma after CAI formation (dashed line, Mishra and Chaussidon, 2014; Nagashima et al., 2015). The accretion timing of the CV3 body which fulfills (i–iii) conditions is about 3.2–3.3 Ma after CAI formation. It is consistent with the accretion timing of the CM2 parent body (Fujiya et al., 2012) but later than those of CO and ordinary parent bodies (Miyamoto et al., 1981; Gopel et al., 1994; Harrison and Grimm, 2010; Doyle et al., 2015).

show Fa<sub>79-96</sub> at their cores (e.g., clast 4 in the Y86009), requiring the fluid pressure of >300 bars during the fayalite formation (Fig. 5). Wilson et al. (1999) concluded that parent bodies of carbonaceous chondrites should have been disrupted if fluid pressure produced during aqueous alteration exceeded the sum of lithostatic pressure and tensile strength of rocks. In order to prevent the disruption of the CV3 chondrite parent body containing fayalite, we assumed a following equation:

$$P_{\text{fluid}} \leq P_{\text{lithostatic}} + \text{Tensile Strength} \quad (2)$$

where  $P_{\text{lithostatic}}$  is lithostatic pressure,  $P_{\text{fluid}}$  is fluid pressure, and Tensile Strength is tensile strength of a rock of ~100 bar (Rubin, 1993). In order to form Fa<sub>79-96</sub> fayalite without disrupting the CV3 body, the Eq. (2) should be satisfied when fluid pressure is  $\geq 300$  bars. If we assume  $P_{\text{fluid}} = 300$  bars, then  $P_{\text{lithostatic}} \geq 300 - 100$  bars = 200 bars. Thus, lithostatic pressure of >200 bars is required to avoid disruption of the CV3 parent body.

In order to produce lithostatic pressure of >200 bars in the CV3 parent body, radius of >110–150 km is needed. This value is calculated by solving the following equation. At each radial distance ( $r$ ) from the center of the body

$$P_{\text{lithostatic}} = 2/3\pi\rho^2G(a^2 - r^2) \quad (3)$$

where  $\rho$  is bulk density,  $G$  is the gravitational constant, and  $a$  is radius of the body (Turcotte and Schubert, 2002). The lithostatic pressure at the center of the body is calculated when  $r = 0$ . In order to produce lithostatic pressure of 200 bars, at the center of the body radius of 110 and 130 km is required, if we assume bulk density of the CV3 parent body containing fayalite is 3500 and 2920 kg/m<sup>3</sup>, respectively. These densities are average grain and bulk density of high density carbonaceous chondrite group, including CV, CO, CK and hydrated metal-rich CR chondrites (Consolmagno et al., 2008). The porosities of these chondrites range from 9.7 to 21.8% (Consolmagno et al., 2008). Whereas, a radius of 150 km is required in the CV3 body with the lithostatic pressure of 200 bars at its center, if we assumed the density of CV3 parent body as 2700 kg/m<sup>3</sup>. The density of 2700 kg/m<sup>3</sup> is calculated under the assumption that water/rock mass ratio of the CV3 body is 0.1 (fayalite formation condition in the CV3<sub>OXB</sub> Bali, Zolotov et al., 2006), and densities of rock and water are 3300 kg/m<sup>3</sup> (Fa<sub>20</sub> olivine) and 1000 kg/m<sup>3</sup> (water), respectively (for details, see Wakita and Sekiya (2011)).

#### 4.4. Estimation of burial depths of formation of fayalite with different compositions

The fluid pressure-dependence on the Fa# of fayalite formed during aqueous alteration (Fig. 5) makes it possible to estimate the burial depths at which fayalites of different compositions formed. According to the discussion above, fayalites showing Fa<sub>79-96</sub> at their cores formed within a CV3 parent body having a radius of at least 110–150 km. Fayalites having higher Fa# should have formed in the outer portions of the body. For example, formation depths of (i) Fa<sub>97</sub> with Fa# zoning (e.g., clast 2 in the Y-86009) and (ii) compositionally pure Fa<sub>100</sub> fayalite without Fa# zoning

(e.g., clast 1 in the Y-86009) could be estimated to be (i) 27 to 60 km below the surface of the CV3 body (lithostatic pressure of 100–200 bars) and (ii) 1 to 3 km below the surface toward the surface layers of the CV3 body (lithostatic pressure of 0–10 bars), respectively, by the following calculation. In order to form fayalite of (i), fluid pressure of 200–300 bars is required during the Fa<sub>97</sub> fayalite formation as previously described (upper arrows in Fig. 5). Whereas, in order to form Fa<sub>100</sub>, fluid pressure of 3–10 bars are needed (lower arrows in Fig. 5). Zolotov et al. (2006) reported that at the time of fayalite formation the likely fluid pressure is close to its maximum pressure (i.e., the sum of the lithostatic pressure and the tensile strength of rock), and thus we could assume following equation:

$$P_{\text{fluid}} = P_{\text{lithostatic}} + \text{Tensile strength} \quad (4)$$

Because fayalite formed under the gas or gas + fluid environment (Zolotov et al., 2006),  $P_{\text{fluid}} \geq P_{\text{lithostatic}}$  is needed in order to present gas and/or fluid in the rock. If  $P_{\text{fluid}} = 200$ –300 bars (necessary fluid pressure of fayalite formation of (i)), then  $P_{\text{lithostatic}} = 200$ –300 bars – 100 bars (tensile strength of rock) = 100–200 bars. This means that fluid pressure of  $P_{\text{fluid}} = 200$ –300 bars exists at  $P_{\text{lithostatic}} = 100$ –200 bars. These lithostatic pressures correspond to 27 to 60 km from the surface of the 200 km sized CV3 body based on the equation (2), if the bulk density of the CV3 body is assumed to be 2700 kg/m<sup>3</sup>.

If  $P_{\text{fluid}} < \text{Tensile Strength}$  of 100 bars (Rubin, 1993),  $P_{\text{lithostatic}}$  appear < 0 from Eq. (3). This means that fluid pressure below Tensile Strength could exist up to the surface (at 0 lithostatic pressure). Thus, if  $P_{\text{fluid}} = 3$ –10 bars (necessary fluid pressure of fayalite formation of (ii)), fluid could formally exist within rock from the depths of lithostatic pressure of 3–10 bars (1–3 km from the surface) up to the surface under the assumption of the bulk density of the CV3 body is 2700 kg/m<sup>3</sup> (Wakita and Sekiya, 2011). Calculated results of fluid pressure, temperature and possibly-formed Fa# of fayalite at each lithostatic pressure (burial depths) are summarized in Table 3.

Finally, we note that these calculations of parent body sizes and burial depths of fayalite formation depend critically on the bulk porosity and permeability of the CV3 chondrite parent body. However, these properties are not well known and we may need to update our calculations if these physical properties are more accurately determined.

#### 4.5. Implication for an accretion time difference of chondrite parent bodies around snow-line areas in the solar nebula

The accretion timing of the chondrite parent bodies has been estimated in earlier studies. For example, the accretion time of the CM2 parent body was estimated to be about 3.0–3.5 Ma after CAI formation from their peak temperatures and Mn–Cr ages of aqueously-formed CM calcite (Fujiya et al., 2012). The accretion time of the CO chondrite parent body was constrained to be 2.1–2.4 Ma after CAI formation based on its peak temperature and Mn–Cr ages of aqueously-formed fayalite (Doyle et al., 2015). The accretion time of the ordinary chondrite parent body was estimated to be ~2–3 Ma after CAI formation based on

Table 3

Fluid and gas pressure, temperature and possibly-formed Fa# of fayalite at each lithostatic pressure (burial depths from the surface) in a CV3 parent body with radius of 200 km.

| Lithostatic pressure [bars] | Burial depths from the surface [km] <sup>a</sup> | Fluid and gas pressure [bars] <sup>b</sup> | T [°C] during aqueous alteration <sup>c</sup> | Possibly-formed Fa# <sup>d</sup> |
|-----------------------------|--|--|---|----------------------------------|
| 0                           | 0  | 0–100                                      | <–100   | No fayalite formed               |
| 3                           | 1  | 3–103                                      | –100 to 160                                   | 88–100                           |
| 10                          | 3  | 10–110                                     | –50 to 200                                    | 88–99                            |
| 100                         | 27   | 100–200                                    | 0–250   | 88–98                            |
| 200                         | 60   | 200–300                                    | 0–280   | 88–97                            |

<sup>a</sup> Burial depth at each lithostatic pressure is calculated from the Eq. (2) under the assumption that bulk density of CV3 parent bodies is 2700 kg/m<sup>3</sup>.

<sup>b</sup> Fluid and gas pressure at each lithostatic pressure is calculated from the Eq. (3).

<sup>c</sup> Temperature range at each lithostatic pressure is estimated from Fig. 7.

<sup>d</sup> Possibly-formed Fa# of fayalite at fluid pressure and temperature during aqueous alteration is estimated from Fig. 5.

thermal modeling, U–Pb ages of phosphates and Mn–Cr ages of aqueously-formed fayalite (Miyamoto et al., 1981; Gopel et al., 1994; Harrison and Grimm, 2010; Doyle et al., 2015). The accretion ages of CV3 chondrite parent body of about 3.2–3.3 Ma after CAI formation (this study) is slightly younger than that of CO and ordinary chondrite parent bodies but is consistent with that of the CM2 parent body (Fig. 9).

Parent bodies of different chondrite groups are thought to have formed at different times and/or locations in the solar nebula with a range of initial ice/dust ratios based on their chondrite properties and mineral components (Zolensky and McSween, 1988; Wood, 2005; Brearley, 2006; Krot et al., 2006; Rubin, 2010, 2011). CV3, CO and ordinary chondrites contain a small amount of secondary minerals that formed during aqueous alteration, suggesting low initial ice/dust ratios when their parent bodies accreted. As the ice/dust ratios would be low near the snow line, parent bodies of CV3, CO and ordinary chondrites might have formed near the snow line (e.g., Wood, 2005). Although CV3 and CO chondrite parent bodies both appear to have formed near the snow line, the CV3 chondrite parent body is estimated to have formed later than the CO and ordinary chondrite parent bodies. On the other hand, CM2 chondrites contain a large amount of secondary minerals, implying that their parent bodies accreted well beyond the snow line with high initial ice/dust ratios (e.g., Wood, 2005). Yet the accretion time of the CM2 chondrite parent body is consistent with that of the CV3 chondrite parent body, suggesting that accretion of the CM2 parent body beyond the snow line occurred at the same time with that of the CV3 body near the snow line despite their differing initial ice/dust ratios.

Two main models have been proposed for the accretion of planetesimals (chondrite parent bodies): (i) mass accretion of gravitationally bound cluster of dust and ice and (ii) collisional growth of dust and ice (Johansen et al., 2007; Wada et al., 2008). A time difference of planetesimal formation at the inner and outer regions of the solar nebula was proposed only by the former model; it takes longer time to form planetesimals in the outer nebular regions rather than the inner nebular regions because of lower surface density in the outer regions of the nebula. Thus, the inferred accretion time difference of CV3, CO, CM2 and

ordinary chondrite parent bodies is consistent with the planetesimal formation model by gravitational/streaming instability. According to this model, the parent body of CV3 chondrites should have formed before the CM2 body since it likely formed closer to the Sun, assuming they have similar sizes. In order to explain the contemporaneous accretion timing of CV3 and CM2 bodies, sizes of CV3 bodies might be smaller than those of CM2 bodies. Further studies would be needed to confirm this suggestion.

## 5. CONCLUSIONS

We determined the formation ages of fayalite occurring in different clasts and/or bulk samples of CV3 carbonaceous chondrites. Fayalite in individual clasts and within different samples showed different compositional trends, suggesting formation at specific temperatures and pressures before incorporation into present structures. Regardless of their formation conditions, all fayalite show a narrow range of the inferred initial <sup>53</sup>Mn/<sup>55</sup>Mn ratios of (1–2) × 10<sup>–6</sup>. Based on the model simulations which satisfy the ages, temperatures and fluid pressure during fayalite formation, and peak metamorphic temperature of CV3<sub>OXA</sub> chondrites, we determined that the CV3 chondrite parent body was at least 110–150 km in radius and accreted 3.2–3.3 Ma after CV3 CAIs. As the CV3 parent body accreted <1 Ma after CV3 chondrule formation, the estimated accretion age is consistent with the radial diffusion model. The CV3 parent body accreted slightly later than the CO and ordinary chondrite parent bodies but contemporaneously with the CM2 parent body. The accretion time of CV3, CO and ordinary chondrite parent bodies implies an accretion time difference near the snow line. The identical accretion timing of CV3 and CM2 chondrite parent bodies suggests that the CM2 chondrite parent body grew to greater size than the CV3 parent body. The obtained accretion time difference between CV3, CO, CM2 and ordinary chondrite parent bodies is consistent with the planetesimal formation model by gravitational/streaming instability.

## ACKNOWLEDGEMENTS

The meteoritic samples of Y86009, A881317, MET01074 and MET00430 were provided by National Institute of Polar Research,

Japan and NASA Johnson Space center. The manuscript was improved by constructive comments from Dr. Nagahara and review by Dr. A. N. Krot. Thermal modelling was carried out on the PC cluster at the Center for Computational Astrophysics, National Astronomical Observatory of Japan. We thank Dr. Ikeda for the support to use JEOL-5800LV SEM and Mr. Shimada for technical assistance in the use of JEM-733 EPMA at Kyushu University. We also thank Dr. Nagahara for the support and Mr. Yoshida for their technical assistance in the use of JSM-7000F FE-SEM at the University of Tokyo. We also thank Dr. K. R. Ludwig for providing the Isoplot/Ex program for Mn–Cr age calibration. This work was supported by Korea Polar Research Institute project PM16030 and JSPS Grant-in-Aid for Scientific Research(S) Grant Number 22224010. M. Zolotov was supported by NASA Cosmochemistry grant NNX14AG19G. S. Messenger was supported by a NASA Cosmochemistry grant.

#### APPENDIX A. SUPPLEMENTARY DATA

Supplementary data associated with this article can be found, in the online version, at <http://dx.doi.org/10.1016/j.gca.2016.11.027>.

#### REFERENCES

- Bland P. A., Jackson M. D., Coker R. F., Cohen B. A., Webber J. B. W., Lee M. R., Duffy C. M., Chater R. J., Ardakani M. G., McPhail D. S., McComb D. W. and Benedix G. K. (2009) Why aqueous alteration in asteroids was isochemical: high porosity  $\neq$  high permeability. *Earth Planet. Sci. Lett.* **287**, 559–568.
- Bland P. A., Collins G. S., Davison T. M., Abreu N. M., Ciesla F. J., Muxworthy A. R. and Moore J. (2014) Pressure–temperature evolution of primordial solar system solids during impact-induced compaction. *Nat. Commun.* **5**, 1–13.
- Bonal L., Quirico E., Bourot-Denise M. and Montagnac G. (2006) Determination of the petrologic type of CV3 chondrites by Raman spectroscopy of included organic matter. *Geochim. Cosmochim. Acta* **70**, 1849–1863.
- Brearley A. J. (1997) Disordered biopyriboles, amphibole, and talc in the Allende meteorite: products of nebular or parent body aqueous alteration? *Science* **276**, 1103–1105.
- Brearley A. J. (1999) Origin of graphitic carbon and pentlandite in matrix olivines in the Allende meteorite. *Science* **285**, 1380–1382.
- Brearley A. J. (2006) The action of water. In *Meteorites and the Early Solar System II* (eds. D. S. Lauretta and J. R. H. Y. McSween). University of Arizona Press, Tucson, AZ, pp. 587–624.
- Brearley A. J. and Krot A. N. (2013) Metasomatism in the early Solar System: the record from chondritic meteorites. In *Metasomatism and the Chemical Transformation of Rock* (eds. D. E. Harlov and H. Austrheim). Springer, Heidelberg, pp. 659–790.
- Buening D. K. and Buseck P. R. (1973) Fe–Mg lattice diffusion in olivine. *J. Geophys. Res.* **78**, 6852–6862.
- Busemann H., Alexander M. O. and Nittler L. R. (2007) Characterization of insoluble organic matter in primitive meteorites by micro Raman spectroscopy. *Meteorit. Planet. Sci.* **42**, 1387–1416.
- Carpenter L., Weiss B. P., Elkins-Tanton L. T., Shuster D. L., Ebel D. and Gattacceca J. (2011) Magnetic evidence for a partially differentiated carbonaceous chondrite parent body. *Proc. Natl. Acad. Sci. USA* **108**, 6386–6389.
- Chakraborty S. (1997) Rates and mechanisms of Fe–Mg interdiffusion in olivine at 980–1300 °C. *J. Geophys. Res.* **102**, 12317–12331.
- Chakraborty S., Farver J. R., Yund R. A. and Rubie D. C. (1994) Mg tracer diffusion in synthetic forsterite and San Carlos olivine as a function of P, T and fO<sub>2</sub>. *Phys. Chem. Miner.* **21**, 489–500.
- Chaumard N. and Devouard B. (2016) Chondrules in CK carbonaceous chondrites and thermal history of the CV–CK parent body. *Meteorit. Planet. Sci.* **51**, 547–573.
- Chaumard N., Devouard B., Bouvier A. and Wadhwa M. (2014) Metamorphosed calcium–aluminum–rich inclusions in CK carbonaceous chondrites. *Meteorit. Planet. Sci.* **49**, 419–452.
- Choi B., Krot A. N. and Wasson J. T. (2000) Oxygen-isotopes in magnetite and fayalite in CV chondrites Kaba and Mokoia. *Meteorit. Planet. Sci.* **35**, 1239–1248.
- Ciesla F. J. and Cuzzi J. N. (2006) The evolution of the water distribution in a viscous protoplanetary disk. *Icarus* **181**, 178–204.
- Connelly J. N., Bizzarro M., Krot A. N., Nordlund Å., Wielandt D. and Ivanova M. A. (2012) The absolute chronology and thermal processing of solids in the solar protoplanetary disk. *Science* **338**, 651–655.
- Consolmagno G., Britt D. and Macke R. (2008) The significance of meteorite density and porosity. *Chem. Erde* **68**, 1–29.
- Cuzzi J. N. and Zahnle K. J. (2004) Material enhancement in protoplanetary nebulae by particle drift through evaporation fronts. *Astrophys. J.* **614**, 490–496.
- Cuzzi J. N., Hogan R. C. and Bottke W. F. (2010) Towards initial mass functions for asteroids and Kuiper Belt Objects. *Icarus* **208**, 518–538.
- Cyr K. E., Sears W. D. and Lunine J. I. (1998) Distribution and evolution of water ice in the solar nebula: implications for Solar System body formation. *Icarus* **135**, 537–548.
- Doyle P. M., Jogo K., Nagashima K., Krot A. N., Wakita S., Ciesla F. and Hutcheon I. (2015) Early aqueous activity on the ordinary and carbonaceous chondrite parent asteroids recorded by fayalite. *Nat. Commun.* **6**, 7444.
- Elkins-Tanton L. T., Weiss B. P. and Zuber M. T. (2011) Chondrites as samples of differentiated planetesimals. *Earth Planet. Sci. Lett.* **305**, 1–10.
- Fu R. R. and Elkins-Tanton L. T. (2014) The fate of magmas in planetesimals and the retention of primitive chondritic crusts. *Earth Planet. Sci. Lett.* **390**, 128–137.
- Fujiya W., Sugiura N., Hotta H., Ichimura K. and Sano Y. (2012) Evidence for the late formation of hydrous asteroids from young meteoritic carbonates. *Nat. Commun.* **3**, 1–6.
- Gopel C., Manhès G. and Allegre C. J. (1994) U–Pb systematics of phosphates from equilibrated ordinary chondrites. *Earth Planet. Sci. Lett.* **121**, 153–171.
- Greenwood R. C., Franchi I. A., Kearsley A. T. and Alard O. (2010) The relationship between CK and CV chondrites. *Geochim. Cosmochim. Acta* **74**, 1684–1705.
- Harrison K. P. and Grimm R. E. (2010) Thermal constraints on the early history of the H-chondrite parent body reconsidered. *Geochim. Cosmochim. Acta* **74**, 5410–5423.
- Hayashi C. (1981) Structure of the solar nebula, growth and decay of magnetic fields and effects of magnetic and turbulent viscosities on the nebula. *Prog. Theor. Phys. Suppl.* **70**, 35–53.
- Holland T. J. B. and Powell R. (1998) An internally consistent thermodynamic data set for phases of petrological interest. *J. Metamorph. Geol.* **16**, 309–343.
- Hua X. and Buseck P. R. (1995) Fayalite in the Kaba and Mokoia carbonaceous chondrites. *Geochim. Cosmochim. Acta* **59**, 563–578.

- Hua X., Huss G. R., Tachibana S. and Sharp T. G. (2005) Oxygen, silicon, and Mn–Cr isotopes of fayalite in the Kaba oxidized CV3 chondrite: constraints for its formation history. *Geochim. Cosmochim. Acta* **69**, 1333–1348.
- Hutcheon I. D., Krot A. N., Keil K., Phinney D. L. and Scott E. R. D. (1998)  $^{53}\text{Mn}$ – $^{53}\text{Cr}$  dating of fayalite formation in the CV3 chondrite Mokoia: evidence for asteroidal alteration. *Science* **282**, 1865–1867.
- Hutcheon I. D., Marhas K. K., Krot A. N., Goswami J. N. and Jones R. H. (2009)  $^{26}\text{Al}$  in plagioclase-rich chondrules in carbonaceous chondrites: evidence for an extended duration of chondrule formation. *Geochim. Cosmochim. Acta* **73**, 5080–5099.
- Hutchison R. (2007) *Meteorites: A Petrologic, Chemical and Isotopic Synthesis*. Cambridge University Press, Cambridge.
- Ikeda Y. and Kimura M. (1995) Anhydrous alteration of Allende chondrules in the solar nebula I Description and alteration of chondrules with known oxygen-isotopic components. In *Proceedings of the NIPR Symposium on Antarctic Meteorites* **8**, 97–122.
- Irving A. J., Larson T. E., Longstaffe F. J., Rumble D., Bunch T. E., Wittke J. H. and Kuehner S. M. (2004) A primitive achondrite with oxygen isotopic affinities to CV chondrites: Implications for differentiation and size of the CV parent body. *American Geophysical Union P31C-02* (abstr.).
- Ito M. and Ganguly J. (2006) Diffusion kinetics of Cr in olivine and  $^{53}\text{Mn}$ – $^{53}\text{Cr}$  thermochronology of early solar system objects. *Geochim. Cosmochim. Acta* **70**, 799–809.
- Jarosewich E. (1990) Chemical analyses of meteorites: a compilation of stony and iron meteorite analyses. *Meteoritics* **25**, 323–337.
- Jogo K., Nakamura T., Noguchi T. and Zolotov M. Y. (2009) Fayalite in the Vigarano CV3 carbonaceous chondrite: occurrences, formation age and conditions. *Earth Planet. Sci. Lett.* **287**, 320–328.
- Jogo K., Nagashima K., Hutcheon I. D., Krot A. N. and Nakamura T. (2013) Heavily metamorphosed clasts from the CV chondrite breccias Mokoia and Yamato-86009. *Meteorit. Planet. Sci.* **47**, 2251–2268.
- Johansen A., Oishi J. S., Mac Low M., Klahr H., Henning T. and Youdin A. (2007) Rapid planetesimal formation in turbulent circumstellar disks. *Nature* **448**, 1022–1025.
- Keller L. P., Thomas K. L., Clayton R. N., Mayeda T. K., DeHart J. M. and McKay D. S. (1994) Aqueous alteration of the Bali CV3 chondrite: Evidence from mineralogy, mineral chemistry, and oxygen isotopic compositions. *Geochim. Cosmochim. Acta* **58**, 5589–5598.
- Kimura M. and Ikeda Y. (1995) Anhydrous alteration of Allende chondrules in the solar nebula II: Alkali-Ca exchange reactions and formation of nepheline, sodalite and Ca-rich phases in chondrules. *Proceedings of the NIPR Symposium on Antarctic Meteorites* **8**, 123–138.
- Kita N. T. and Ushikubo T. (2012) Evolution of protoplanetary disk inferred from  $^{26}\text{Al}$  chronology of individual chondrules. *Meteorit. Planet. Sci.* **47**, 1108–1119.
- Kita N. T., Yin Q., MacPherson G. J., Ushikubo T., Jacobsen B., Nagashima K., Kurahashi E., Krot A. N. and Jacobsen S. B. (2012)  $^{26}\text{Al}$ – $^{26}\text{Mg}$  isotope systematics of the first solids in the early solar system. *Meteorit. Planet. Sci.* **48**, 1383–1400.
- Krot A. N., Scott E. R. D. and Zolensky M. E. (1995) Mineralogical and chemical modification of components in CV3 chondrites: nebular or asteroidal processing? *Meteoritics* **30**, 748–775.
- Krot A. N., Petaev M. I., Scott E. R. D., Choi B., Zolensky M. E. and Keil K. (1998) Progressive alteration in CV3 chondrites: more evidence for asteroidal alteration. *Meteorit. Planet. Sci.* **33**, 1065–1085.
- Krot A. N., Meibom A. and Keil K. (2000) A clast of Bali-like oxidized CV material in the reduced CV chondrite breccia Vigarano. *Meteorit. Planet. Sci.* **35**, 817–825.
- Krot A. N., Petaev I. M. and Bland P. A. (2004) Multiple formation mechanisms of ferrous olivine in CV carbonaceous chondrites during fluid-assisted metamorphism. *Antarct. Meteorit. Res.* **17**, 153–171.
- Krot A. N., Hutcheon I. D., Brearley A. J., Pravdivtseva O. V., Petaev M. I. and Hohenberg C. M. (2006) Timescales and setting for alteration of chondritic meteorites. In *Meteorites and the Early Solar System II* (eds. D. S. Lauretta and , Jr.H. Y. McSween). University of Arizona Press, Tucson, AZ, pp. 525–553.
- Lodders K. (2003) Solar system abundances and condensation temperatures of the elements. *Astrophys. J.* **591**, 1220–1247.
- MacPherson G. J. and Krot A. N. (2014) The formation of Ca-, Fe-rich silicates in reduced and oxidized CV chondrites: The roles of impact-modified porosity and permeability, and heterogeneous distribution of water ices. *Meteorit. Planet. Sci.* **49**, 1250–1270.
- MacPherson G. J., Davis A. M. and Zinner E. K. (1995) The distribution of aluminum-26 in the early Solar System—A reappraisal. *Meteoritics* **30**, 365–386.
- McKibbin S. J., Ireland T. R., Amelin Y., O’Neill H., St C. and Holden P. (2013) Mn–Cr relative sensitivity Factors for Secondary Ion Mass Spectrometry analysis of Mg–Fe–Ca olivine and implications for the Mn–Cr chronology of meteorites. *Geochim. Cosmochim. Acta* **110**, 216–228.
- H.Y., Jr, McSweeney (1977) Petrographic variations among carbonaceous chondrites of the Vigarano type. *Geochim. Cosmochim. Acta* **41**, 1777–1790.
- Mironenko M. V., Melikhova T. Y., Zolotov M. Y. and Akinfiyev N. N. (2008) GEOCHEQ\_M: program complex for thermodynamic and kinetic modeling of geochemical processes in rock–water–gas systems. Version 2008. Vestnik Otdelenia Nauk o Zemle RAN I.
- Mishra R. K. and Chaussidon M. (2014) Timing and extent of Mg and Al isotopic homogenization in the early inner Solar System. *Earth Planet. Sci. Lett.* **390**, 318–326.
- Miyamoto M., Fujii N. and Takeda H. (1981) Ordinary chondrite parent body: an internal heating model. *Proc. Lunar. Planet. Sci.* **12B**, 1145–1152.
- Morioka M. (1981) Cation diffusion in olivine-II. Ni–Mg, Mn–Mg, Mg and Ca. *Geochim. Cosmochim. Acta* **45**, 1573–1580.
- Nagashima K., Kro A. N. and M. Komatsu. (2015)  $^{26}\text{Al}$ – $^{26}\text{Mg}$  systematics in chondrules from Kaba and Yamato 980145 CV3 chondrites. In *78th Annual Meeting of the Meteoritical Society*, **1856**, pp. 5167 (abstr.).
- Palguta J., Schubert G. and Travis B. J. (2010) Fluid flow and chemical alteration in carbonaceous chondrite parent bodies. *Earth Planet. Sci. Lett.* **296**, 235–243.
- Papanastassiou D. A. (1986) Chromium isotopic anomalies in the Allende meteorite. *Astrophys. J.* **308**, L27–L30.
- Righter K. and Neff K. E. (2007) Temperature and oxygen fugacity constraints on CK and R chondrites and implications for water and oxidation in the early solar system. *Polar Sci.* **1**, 25–44.
- Rubin A. E. (1993) Dikes vs. diapirs in viscoelastic rock. *Earth Planet. Sci. Lett.* **117**, 653–670.
- Rubin A. E. (2010) Physical properties of chondrules in different chondrite groups: Implications for multiple melting events in dusty environments. *Geochim. Cosmochim. Acta* **74**, 4807–4828.
- Rubin A. E. (2011) Origin of the differences in refractory-lithophile-element abundances among chondrite groups. *Icarus* **213**, 547–558.

- Rubin A. E. and Wasson J. T. (1995) Variations of chondrite properties with heliocentric distance. *Meteoritics* **30**, 569 (abstr.).
- Schoenbeck T. W., Kleine T. and Irving A. J. (2006) Chemical and Hf-W isotopic composition of CV metachondrite NWA 3133. *Lunar. Planet. Sci. XXXVII*, #1550 (abstr.).
- Shukolyukov A., Lugmair G. W. and Irving A. J. (2011) Mn–Cr isotope systematics and excess of  $^{54}\text{Cr}$  in metachondrite Northwest Africa 3133. *Lunar Planet Sci. XLII*, #1608 (abstr.).
- Stevenson D. J. and Lunine J. I. (1988) Rapid formation of Jupiter by diffuse redistribution of water vapor in the solar nebula. *Icarus* **75**, 146–155.
- Stracke A., Palme H., Gellissen M., Münker C., Kleine T., Birbaum K., Günther D., Bourdon B. and Zipfel J. (2012) Refractory element fractionation in the Allende meteorite: implications for solar nebula condensation and the chondritic composition of planetary bodies. *Geochim. Cosmochim. Acta* **85**, 114–141.
- Sugiura N., Miyazaki A. and Yanai K. (2005) Widespread magmatic activities on the angrite parent body at 4562 Ma ago. *Earth Planets Space* **57**, 13–16.
- Tomeoka K. and Ohnishi I. (2010) Indicators of parent-body processes: hydrated chondrules and fine-grained rims in the Mokoia CV3 carbonaceous chondrite. *Geochim. Cosmochim. Acta* **74**, 4438–4453.
- Tomeoka K. and Ohnishi I. (2014) Olivine-rich rims surrounding chondrules in the Mokoia CV3 carbonaceous chondrite: Further evidence for parent-body processes. *Geochim. Cosmochim. Acta* **137**, 18–34.
- Tomeoka K. and Tanimura I. (2000) Phyllosilicate-rich chondrule rims in the Vigarano CV3 chondrite: evidence for parent-body processes. *Geochim. Cosmochim. Acta* **64**, 1971–1988.
- Travis B. J. and Schubert G. (2005) Hydrothermal convection in carbonaceous chondrite parent bodies. *Earth Planet. Sci. Lett.* **240**, 234–250.
- Turcotte D. L. and Schubert G. (2002) *Geodynamics*. Cambridge University Press, Cambridge.
- Van Kooten E. M. M. E., Wielandta D., Schiller M., Nagashima K., Thomen A., Larsen K. K., Olsen M. B., Nordlund Å., Krot A. N. and Bizzarro M. (2016) Isotopic evidence for primordial molecular cloud material in metal-rich carbonaceous chondrites. *Proc. Natl. Acad. Sci. USA* **113**, 2011–2016.
- Wada K., Tanaka H., Suyama T., Kimura H. and Yamamoto T. (2008) Numerical simulation of dust aggregate collisions. II. Compression and disruption of three-dimensional aggregates in head-on collisions. *Astrophys. J.* **677**, 1296–1308.
- Wakita S. and Sekiya M. (2011) Thermal evolution of icy planetesimals in the solar nebula. *Earth Planets Space* **63**, 1193–1206.
- Wasson J. T., Isa J. and Rubin A. E. (2013) Compositional and petrographic similarities of CV and CK chondrites: a single group with variations in textures and volatile concentrations attributable to impact heating, crushing and oxidation. *Geochim. Cosmochim. Acta* **108**, 45–62.
- Weisberg M. K., Printz M., Clayton R. and Mayeda T. K. (1997) CV3 chondrites: three subgroups, not two. *Meteorit. Planet. Sci.* **32**, 138–139.
- Wilson L., Keil K., Browning L. B., Krot A. N. and Bourcier W. (1999) Early aqueous alteration, explosive disruption, and re-processing of asteroids. *Meteorit. Planet. Sci.* **34**, 541–557.
- Wood J. A. (2005) The chondrite types and their origins. In *Chondrites and the Protoplanetary Disk* (eds. A. N. Krot, E. R. D. Scott and B. Reipurth). Astronomical Society of the Pacific, San Francisco, CA, pp. 953–971.
- Young E. D. (2001) The hydrology of carbonaceous chondrite parent bodies and the evolution of planet progenitors. *Phil. Trans. R. Soc. Lond. A* **359**, 2095–2110.
- Zolensky M. and McSween, Jr, H. Y. (1988) Meteorites and the early solar system (eds. J. F. Kerridge and M. S. Matthews). University of Arizona Press, Tucson, AZ, pp. 114–143.
- Zolotov M. Y., Mironenko M. V. and Shock E. L. (2006) Thermodynamic constraints on fayalite formation on parent bodies of chondrites. *Meteorit. Planet. Sci.* **41**, 1775–1796.

Associate editor: Alexander N. Krot